Astronomy & Astrophysics manuscript no. Methanol_landscape_accepted
October 13, 2020

Polarization properties of methanol masers

D. Dall'Olio[1], W. H. T. Vlemmings[1], B. Lankhaar[1], and G. Surcis[2]

[1] Department of Space, Earth and Environment, Chalmers University of Technology, Onsala Space Observatory, Observatorievägen 90, 43992 Onsala, Sweden; e-mail: daria.dallolio@chalmers.se
[2] INAF–Osservatorio Astronomico di Cagliari, Via della Scienza 5, 09047 Selargius, Italy

Received giorno mese anno; accepted giorno mese anno

ABSTRACT

Context. Astronomical masers have been effective tools to study magnetic fields for many years. Observing the linear and circular polarization of different maser species allows the determination of magnetic field properties, such as morphology and strength. In particular, methanol can be used to probe different parts of protostars such as accretion discs and outflows, since it produces one of the strongest and the most commonly observed masers in massive star-forming regions.
Aims. We investigate the polarization properties of selected methanol maser transitions in light of newly calculated methanol Landé g-factors and considering hyperfine components. We compare our results with previous observations and we evaluate the effect of preferred hyperfine pumping and non-Zeeman effects.
Methods. We run simulations using the radiative transfer code CHAMP for different magnetic field values, hyperfine components and pumping efficiencies.
Results. We find a dependence of the linear polarization fraction on the magnetic field strength and on hyperfine transitions. The circular polarization fraction also shows a dependence on the hyperfine transitions. Preferred hyperfine pumping can explain some high levels of linear and circular polarization and some of the peculiar features seen in the S-shape of observed V-profiles. By comparing some methanol maser observations taken from the literature with our simulations, we find that the observed methanol masers are not significantly affected by non-Zeeman effects related to the competition between stimulated emission rates and Zeeman rates, like the rotation of the symmetry axis. We consider also the relevance of other non-Zeeman effects that are likely active for modest saturation levels, like the effect of magnetic field changes along the maser path and anisotropic resonant scattering.
Conclusions. Our models show that for methanol maser emission, both the linear and circular polarization percentages depend on which hyperfine transition is masing and the degree to which it is being pumped. Since non-Zeeman effects become more relevant at high values of brightness temperatures, it is important to obtain good estimates of these quantities and on maser beaming angles. Better constraints on the brightness temperature will help in understand about the extent to which non-Zeeman effects contribute to the observed polarization percentages. In order to detect separate hyperfine components, an intrinsic thermal line width significantly smaller than the hyperfine separation is required.

Key words. masers – polarization – Stars: formation – magnetic fields

1. Introduction

The role of magnetic field during star formation has been a topic of great debate for years. Many observations have been performed trying to detect magnetic field morphology and strength towards star forming regions. Several works have already demonstrated that astrophysical masers are powerful tools to investigate magnetic field properties in young protostars (recently reviewed by Crutcher & Kemball 2019, and references therein). Through the study of linearly and circularly polarized maser emission, it is possible to obtain information about the magnetic field, such as direction and strength, over spatial scales of 10-100 au (e.g. Vlemmings et al. 2010; Surcis et al. 2013). Moreover, different maser species and transitions probe different regions of the protostar, providing a unique picture of the physical conditions of the material where star formation processes are ongoing (Surcis et al. 2011a). Masers can also help to investigate the link between the gas properties and the magnetic field: for instance, maser polarization observations were used to infer a relationship between the density of the gas and the magnetic field acting in the region (Fish et al. 2006; Vlemmings 2008). Maser polarization observations have also been used to infer properties of the large scale Galactic magnetic field (e.g. Green et al. 2012).

Circular polarization has been detected in the majority of the maser species such as hydroxyl, water and methanol (Etoka et al. 2005; Vlemmings et al. 2006; Sarma et al. 2008; Surcis et al. 2011b; Caswell et al. 2011; Hunter et al. 2018), and in particular methanol masers have emerged as excellent tools to probe magnetic fields during star formation (e.g. Vlemmings 2008; Surcis et al. 2019; Momjian & Sarma 2019; Sarma & Momjian 2020, and references therein). Although the circularly polarized emission of methanol maser has been regularly detected, no exact estimates of the magnetic field strength were possible due to unknown Landé g-factors (Vlemmings et al. 2011). Thanks to the recent detailed calculations of the Landé g-factors for all methanol transitions and the associated hyperfine components (Lankhaar et al. 2016, 2018), it is now possible to obtain a complete interpretation of the methanol maser polarization properties and infer the magnetic field characteristics.

In this paper we investigate the methanol maser polarization properties using the maser polarization radiative transfer code CHAMP (Lankhaar & Vlemmings 2019), performing several simulations of different methanol masers transitions, as described in Sect. 2. We report our results for the different masers transitions in Sect. 3, with a more detailed view on the 6.7 GHz

one given the large amount of observations in the literature, and with a more general description of the most important features observed at other frequencies. Then, in Sect. 4 we compare the results of our simulations with previous observations and we discuss the importance of hyperfine preferred pumping, its effect on the polarization fraction and the V spectra, and the presence of non-Zeeman effects. In Sect. 5 we present our conclusions and future perspectives, considering that this work can be the starting point for a larger and more detailed study of magnetic fields, and that further high-resolution observations will help to better understand the action of preferred hyperfine pumping.

1.1. Origin of circular polarization and non-Zeeman effects

One of the major sources of circular polarization of molecular lines is the Zeeman effect (Zeeman 1897; Fiebig & Guesten 1989; Sarma et al. 2001). According to the theory, under the action of a magnetic field B, the emission from a molecule is separated in several components due to the magnetic sub-levels. The shift between these components is named Zeeman splitting and can be used to derive the amount of circular polarization, which is proportional to the magnetic field strength. Studying circular polarization in maser emissions is therefore fundamental to infer the magnetic field strength of the masing region.

In general, the saturation level and the nature of the masing molecule (paramagnetic or non-paramagnetic) are the main factors responsible for the maser polarization properties (e.g. Watson 2008; Dinh-v-Trung 2009). In addition, maser polarization is also affected by the ratio between the Zeeman frequency $g\Omega$, the rate of stimulated emission R and the decay rate of the molecular state Γ (Western & Watson 1984).

The rate of stimulated emission can be obtained from

$$R \simeq \frac{AkT_B\Delta\Omega}{4\pi h\nu} \quad , \tag{1}$$

where A is the Einstein coefficient which depends on the hyperfine transition, k and h are the Boltzmann and Planck constants respectively, ν is the maser frequency. T_B and $\Delta\Omega$ are the maser brightness temperature and beaming solid angle (see also Vlemmings et al. 2011).

The Zeeman frequency is defined as

$$g\Omega = \frac{2g\mu B}{\hbar} \quad , \tag{2}$$

where B is the magnetic field in G, $\hbar$ is the reduced Planck constant and g is the Landé g-factor (see e.g. Nedoluha & Watson 1990b). In case of paramagnetic molecule (e.g. OH) μ is the Bohr magneton ($\mu_B = e\hbar/2m_ec$) while in case of non-paramagnetic molecule (e.g. H_2O or CH_3OH) it is the nuclear magneton ($\mu_N = e\hbar/2m_nc$), where e is the electron charge, m_e and m_n are the electron and nucleon mass respectively.

The magnitude of the Zeeman effect depends on $g\Omega$ and it is different between paramagnetic and non-paramagnetic molecules. Since $\mu_B/\mu_N \sim 10^3$, paramagnetic molecules can show a split three orders of magnitude larger than the non-paramagnetic ones (Vlemmings 2007). Moreover, for paramagnetic molecules, the Zeeman frequency $g\Omega$ is usually larger than the intrinsic line width; thus the Zeeman components are separated and resolved and from the Zeeman splitting it is possible to obtain the magnetic field along the line of sight without ambiguity, $B_{\parallel} = B\cos\theta$, with θ defined as the angle between the magnetic field and the line of sight. On the contrary, for non-paramagnetic molecules like methanol, $g\Omega$ is smaller than the line width, and the Zeeman components overlap. In this case it is more complicated to infer circular polarization measurements, because it also depends on the saturation level and non-Zeeman effects might arise, compromising the measurement of the regular Zeeman splitting. A maser is defined saturated when the rate of stimulated emission R exceeds the decay rate of the involved molecular state Γ.

1.1.1. Rotation of the symmetry axis

When $g\Omega > R$, the magnetic field direction is the quantization axis, but when the maser brightness increases or for weak B, R can become much larger than $g\Omega$ and a rotation of the symmetry axis can occur. This change of quantization axis can generate an intensity-dependent circular polarization similar to the regular Zeeman splitting (Nedoluha & Watson 1990a). Therefore, it is important to know when this effect might occur, by estimating R and $g\Omega$. The ratio between the Zeeman splitting rate and the stimulated emission rate is

$$\frac{R}{g\Omega} \simeq 1.7\frac{1}{g}\frac{[\mathrm{mG}]}{B}\frac{T_b}{[10^{10}\mathrm{K}]}\frac{\Delta\Omega}{[10^{-2}\mathrm{sr}]}\frac{[\mathrm{GHz}]}{\nu}\frac{A}{[10^{-7}\mathrm{s}^{-1}]}. \tag{3}$$

The rotation of the symmetry axis might occur when $\frac{R}{g\Omega} > 1$. In the case of the 6.7 GHz methanol maser, considering the typical values for the beaming solid angle $\Delta\Omega = 10^{-2}$ K sr, a magnetic field $B = 10$ mG, $A = 1.074 \times 10^{-9}$ s^{-1} and an average Landé factor calculated using all hyperfine components $g_a = 0.236$ (Lankhaar et al. 2016), this effect might arise only when the maser is deeply saturated, with $T_B \geq 10^{12}$ K. This result also holds when considering the largest and the smallest g-factor of the 6.7 GHz methanol maser hyperfine transition $3 \rightarrow 4$A and $5 \rightarrow 6$B respectively, leading to $T_B \geq 10^{10}$ K.

1.1.2. Effect of magnetic field changes

There are also other non-Zeeman mechanisms that can generate high levels of polarization at lower T_B. One of these effects is due to magnetic field changes along the maser path, for example a rotation (Wiebe & Watson 1998). This rotation converts the linear polarization fraction P_L to circular polarization fraction P_V. Considering a rotation of 1 rad in the magnetic field direction along the maser path, the fractional circular polarization generated by this mechanism is $P_L^2/4$. According to previous observations of 6.7 GHz methanol masers, this mechanism only produces minor contributions (Vlemmings et al. 2011). For example, the polarization observed in high angular resolution observations for 6.7 GHz masers ranges usually from 1% to 4%. Therefore the change of magnetic field direction along the maser propagation direction can contribute at most $\sim 0.04\%$, that is only a fraction of the observed values of P_V (e.g. Surcis et al. 2009, 2012, 2019). But this effect can be important for very high levels of linear polarization $P_L \sim 10\%$, causing an extra $P_V \sim 0.25\%$. Recent methanol maser observations by Breen et al. (2019) have registered a level of linear polarization $\sim 7.5\%$, and we will discuss them in Sect. 4.

1.1.3. Anisotropic resonant scattering

Resonant scattering is a higher-order radiation matter interaction that describes the absorption and subsequent immediate emission of a photon by a molecule or atom. Houde et al. (2013) point out that forward resonant scattering is coherent in nature, and

that a large ensemble of molecules, collectively scatter incoming radiation. In the presence of a magnetic field, such collective resonant scattering leads to a significant phase shift between the left and right-circularly polarized radiation modes. This process is called anisotropic resonant scattering (ARS) and leads to the conversion of linear polarization (by way of the Stokes U component) to circular polarization.

Houde (2014) propose that the circular polarization of SiO masers might be generated through the anisotropic resonant scattering of linearly polarized maser radiation by a foreground cloud between the maser and the observer. The foreground cloud may be out of the velocity range of the maser. Alternatively, the collective resonant scattering of radiation might be a feature of the radiative transfer of maser radiation. CHAMP only accounts for first-order radiative interactions and neglects resonant scattering. Proper estimates of the probability of ARS in relation to maser amplification have to be developed before the importance of ARS to maser radiative transfer can be evaluated.

Circular polarization profiles generated through ARS do not necessarily lead to the antisymmetric S-shaped profile that characterizes Zeeman circular polarization. Only under special conditions are antisymmetric Stokes-V profiles generated by ARS. The Stokes-V profiles of methanol masers are generally characterized by an antisymmetric spectrum.

1.1.4. Other non-Zeeman effects

Other non-Zeeman effects might be due to instrumental effects and to the presence of a velocity gradient across an extended source. Potential instrumental effects causing extra circular polarization depend on the instrument characteristics, and are generally reported in the literature. A velocity gradient could originate an S-shaped V spectrum like the one produced by the Zeeman effect, but this effect is rare with masers since they are point-like sources producing narrow spectral lines developing in a narrow velocity range (e.g. Sarma & Momjian 2020).

2. Methods

In order to investigate the polarization of methanol masers by a magnetic field and its effects on the hyperfine structure, we ran simulations using the CHAMP code (Lankhaar & Vlemmings 2019). CHAMP is a maser polarization radiative transfer code that takes into account all dominant hyperfine components of a molecule and their individual Landé factors. CHAMP implements both the methods in Nedoluha & Watson (1992, hereafter N&W92), which do not treat non-Zeeman effects, and those in Nedoluha & Watson (1994, hereafter N&W94), which do consider non-Zeeman effects. The user can choose which method to use. In addition to a combined treatment of all hyperfines according to their transition probabilities, CHAMP includes the possibility *i)* to change the pumping efficiency for different hyperfine components, and *ii)* of anisotropic pumping.

The linear polarization degree is defined as

$$P_L = \frac{\sqrt{Q^2 + U^2}}{I} \quad , \tag{4}$$

the polarization angle is

$$\psi = \frac{1}{2}\,\mathrm{atan}\left(\frac{U}{Q}\right) \quad , \tag{5}$$

and the circular polarization degree is

$$P_V = \frac{(V_{\max} - V_{\min})}{I} \quad , \tag{6}$$

where I, Q, U and V are the Stokes parameters.

The polarization angle is relative to the projection of the magnetic field direction onto the plane of the sky, that we take to be North-South (unless along the maser beam when $\theta = 0°$).

In Table 1 we report the maser transitions that we used in our simulations. Since the size of the masing region or the maser beaming angle $\Delta\Omega$ are often unknown, for comparison with our models we give the value of the brightness temperature T_B assuming a maser spot size of 3 mas. We also give a lower limit for T_B based on the observations from Breen et al. (2019), Sarma & Momjian (2020), Momjian & Sarma (2019), Surcis et al. (2009) and Surcis et al. (2019). In the case of the 12.2 GHz maser, we are not modelling a specific source but we are giving a typical value considering the previous work by Moscadelli et al. (2003). For known spectral features, T_B can be derived using the equation

$$\frac{T_B}{[\mathrm{K}]} = \frac{S(\nu)}{[\mathrm{Jy}]}\left(\frac{\Sigma^2}{[\mathrm{mas}^2]}\right)^{-1} \zeta_\nu \quad , \tag{7}$$

where $S(\nu)$ is the detected flux density, Σ is the maser angular size and ζ_ν is a constant that includes a proportionality factor obtained for a Gaussian shape (Burns et al. 1979) and scales with the frequency according to the relation

$$\zeta_\nu \simeq 6.1305 \times 10^{11}\left(\frac{\nu}{[\mathrm{GHz}]}\right)^{-2} \frac{\mathrm{mas}^2}{\mathrm{Jy}}\mathrm{K} \quad . \tag{8}$$

In Table 1 we also report which method between N&W92 and N&W94 we used. We performed simulations for different methanol maser transitions at different magnetic field strengths, angular momentum transitions, and propagation angles θ. The molecular parameters used in the simulation are presented in Tables A.1– A.13 and are taken from Lankhaar et al. 2018 or, for the newly discovered transitions observed by Breen et al. 2019, computed for this paper. In these Tables, the quantities marked as "g-factors" are defined as $\mu_N g/\hbar$. We ran calculations assuming an intrinsic thermal velocity width $v_{th} = 1$ km s^{-1}. For all the transitions we used a pumping efficiency $\delta = 0.02$, a decay rate of the upper and lower level $\Gamma = 1$ s^{-1} (Vlemmings et al. 2010; Lankhaar & Vlemmings 2019) and, in case of anisotropic pumping, the anisotropy degree $\epsilon = 0.01$. The parameters are described in Lankhaar & Vlemmings 2019.

3. Results

3.1. 6.7 GHz methanol maser

We report on our simulations of the 6.7 GHz methanol maser in a range of different magnetic field strengths (1, 3, 10, 20, 30 and 100 mG), with varying luminosity and magnetic field angles. The results of these simulations are shown in several figures in the body of the paper (Fig. 1– 3) and in the appendix (Fig. A.1– A.15). The magnetic field strength, the thermal velocity width v_{th}, the propagation angle θ and the transition angular momenta are indicated in each figure. In Fig. 1– 3, A.1, and A.6– A.11, the panel at the top left labelled "baseline" indicates a maser emission where all the eight hyperfine transitions contribute equally, while all other panels assume a preferred pumping for the indicated $i \rightarrow j$ transition. The preferred pumping rate is ten times larger than the other transitions' rate.

We present in Fig. 1 the linear and circular polarization fraction P_L and P_V as a function of the maser luminosity for five different θ values. We mark with a vertical line the locus $g\Omega = 10R$, that for 6.7 GHz methanol maser falls at $T_B\Delta\Omega \sim 10^{10}$K sr. For

Table 1: Methanol maser transitions considered in our simulations and observational parameters

Spectral line	Frequency GHz	T_B Lower Limit[a] K	T_B[a] K	Obs. linear pol. %	Obs. circular pol. %	Source and references	code
$CH_3OH\ 17_{-2} \rightarrow 18_{-3}$ E (v_t=1)	6.18	2.2×10^{6}	5.2×10^{11}	7.0	<0.5	G358.931–0.030[b]	N&W92
$CH_3OH\ 5_1 \rightarrow 6_0$ A^+ (v_t=0)	6.68	7.6×10^{6} 2.8×10^{13} 1.3×10^{12}	1.5×10^{12} 8.7×10^{13} 6.3×10^{12}	7.5 8.1 4.5	0.5 2.1 0.2	G358.931–0.030[b], W3(OH)[c], W75N[c]	N&W94
$CH_3OH\ 12_4 \rightarrow 13_3$ A^- (v_t=0)	7.68	4.5×10^{6}	6.5×10^{11}	3.5	<0.5	G358.931–0.030[b]	N&W92
$CH_3OH\ 12_4 \rightarrow 13_3$ A^+ (v_t=0)	7.83	4.5×10^{6}	6.3×10^{11}	3.5	<0.5	G358.931–0.030[b]	N&W92
$CH_3OH\ 2_0 \rightarrow 3_1$ E (v_t=0)	12.2	$10^{9} - 10^{12}$	–	–	–	W3(OH)[d]	N&W94
$CH_3OH\ 17_6 \rightarrow 18_5$ E (v_t=0)	20.3	4.5×10^{4}	1.7×10^{10}	4.0	2.0	G358.931–0.030[e]	N&W92
$CH_3OH\ 10_1 \rightarrow 11_2$ A^+ (v_t=1)	20.9	3.6×10^{4}	1.5×10^{11}	7.0	<0.5	G358.931–0.030[b]	N&W92
$CH_3OH\ 5_2 \rightarrow 5_1$ E (v_t=0)	25.0	9.1×10^{3}	7.2×10^{9}	–	0.3	OMC–1[f]	N&W94
$CH_3OH\ 4_{-1} \rightarrow 3_0$ E	36.2	1.7×10^{1} 3.7×10^{4}	2.6×10^{7} 3.4×10^{9}	<0.5 –	<0.5 0.1	G358.931–0.030[b], M8E[g]	N&W94
$CH_3OH\ 7_{-2} \rightarrow 8_{-1}$ E (v_t=0)	37.7	8.7×10^{3}	1.2×10^{10}	3.5	0.5	G358.931–0.030[b]	N&W92
$CH_3OH\ 7_0 \rightarrow 6_1$ A^+	44.1	1.2×10^{2} 5.0×10^{4}	3.15×10^{8} 1.3×10^{10}	<0.5 –	<0.5 0.05	G358.931–0.030[b], DR21W[h]	N&W94
$CH_3OH\ 2_0 \rightarrow 3_1$ E (v_t=1)	44.9	1.9×10^{4}	1.7×10^{10}	2.5	<0.5	G358.931–0.030[b]	N&W94
$CH_3OH\ 9_3 \rightarrow 10_2$ E (v_t=0)	45.8	1.4×10^{4}	1.3×10^{10}	7.0	1.5	G358.931–0.030[b]	N&W92

Notes. [(a)] Brightness temperature is estimated using a maser spot size of 3 mas using Eq. (7) and Eq. (8), while the lower limit is based on the observational details given in the source references. [(b)] From Breen et al. (2019). [(c)] For W3(OH) we refer to the feature W3OH.22 from Surcis et al. (2019), and for W75N to Surcis et al. (2009). [(d)] We do not model any specific maser but we only report values observed by Moscadelli et al. (2003). [(e)] From MacLeod et al. (2019). [(f)] We used the component 2 of the maser observed by Sarma & Momjian (2020). [(g)] From Sarma & Momjian (2009). [(h)] We used the component 1 of the maser observed by Momjian & Sarma (2019).

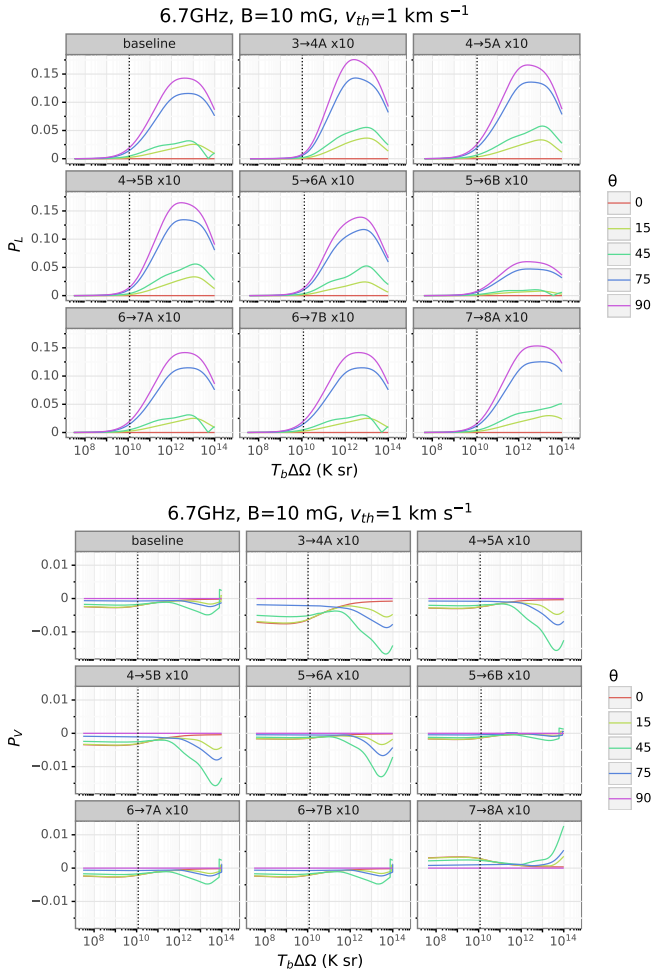

Fig. 1: 6.7 GHz methanol maser linear and circular polarization fraction as a function of the maser luminosity for five different θ. The vertical line marks $T_B\Delta\Omega$ where $g\Omega = 10R$. The magnetic field strength is 10 mG, the thermal velocity width is 1 km s^{-1}, and the preferred hyperfine transitions are indicated in each panel. The panel at the top left labelled "baseline" indicates a fixed pumping rate equal for all the hyperfine transitions, while all others assume a 10× preferred pumping for the indicated $i \rightarrow j$ transition. The results of the simulation performed with other magnetic field strengths are given in Appendix A.

$T_B\Delta\Omega \lesssim 10^{10}$ K sr the Zeeman frequency $g\Omega$ is much higher than the stimulated emission rate R. On the contrary for $T_B\Delta\Omega \gtrsim 10^{10}$ K sr, the Zeeman frequency is similar to or lower than the rate of stimulated emission. As already mentioned in Sect. 1.1, masers can be affected by several non-Zeeman processes that can intensify or generate linear and circular polarization. Usually $g\Omega = 10R$ has been used in the literature (e.g. by Pérez-Sánchez & Vlemmings 2013) to mark the region where non-Zeeman effects become relevant, and therefore inferring magnetic field properties becomes more challenging, because the magnetic field is not directly related to P_L and P_V. One of the most prominent non-Zeeman effects is the rotation of the symmetry axis that can occur when $g\Omega < 10R$ (Pérez-Sánchez & Vlemmings 2013; Wiebe & Watson 1998), thus we decided to indicate $g\Omega = 10R$ as an upper limit for having reliable P_L and P_V.

P_L and P_V show a clear dependence on the hyperfine transitions, on the magnetic field strength and on the angle θ. From these plots it is quite evident that each single hyperfine component is affected by the magnetic field in a different way, and therefore, in presence of preferred hyperfine pumping, we observe a specific level of polarization fraction. At a first glance, these dependencies appear most prominent above $T_B\Delta\Omega$ corresponding to $g\Omega = 10R$, however noticeable effects also occur when $g\Omega > 10R$ for several transitions, such as 3 → 4 A and 4 → 5 A. For example the dependence on θ shown in Fig. A.5 is different from the usual cosθ dependence (Watson & Wyld 2001) also for $T_B\Delta\Omega$ below $g\Omega = 10R$. Also these dependencies seem weaker for P_V compared to that for P_L , unless the magnetic field is very high, ∼100 mG (Fig. A.1), or the hyperfine is preferentially pumped by a large degree,∼ 100 times (Fig. A.3).

We will now consider the P_L and P_V values at $g\Omega = 10R$. When $\theta = 90^o$, and $B = 10$ mG, the maximum linear polarization fraction is found to be of the order of 3% for the hyperfine transition 4 → 5 A. When $\theta = 0^o$ and $B = 10$ mG, we obtain a maximum circular polarization fraction of the order of 1% for the hyperfine transition 3 → 4 A. As the magnetic field strength increases, the position of $g\Omega = 10R$ falls at higher $T_B\Delta\Omega$. Thus, for $B = 100$ mG, P_L can reach 10% in the hyperfine transitions 4 → 5 A at $\theta = 90^o$, while P_V can rise up to 8% when the hyperfine transition 3 → 4 A is preferentially pumped, and $\theta = 0^o$.

We also investigated different degrees of preferred pumping for the two strongest hyperfine transitions 3 → 4 A and 4 → 5 A. We observed that both the linear and circular polarization fractions increase with the preferred pumping. These results are shown in Fig. A.3 and Fig. A.4, where the linear and circular polarization fractions are plotted as a function of the maser luminosity. Different degrees of preferred pumping are shown in different colours for the two hyperfine transitions, assuming a magnetic field of 10 mG. The vertical dotted lines indicate when $g\Omega = 10R$.

In Tables 2 and 3, we report the P_L and P_V values taken at $g\Omega = 10R$, for all the masers and for a magnetic field $B = 10$ mG. The results of the simulation performed with other magnetic field strengths (1 and 100 mG) are given in Appendix A in Fig. A.1.

In Fig. 2 and from top to bottom, respectively, we plot the linear polarization fraction P_L, the circular polarization fraction P_V and the linear polarization angle ψ as a function of the propagation angle θ and of the rate of stimulated emission for a magnetic field of 10 mG. These plots are symmetric along the line $\theta = 90°$. The results of the simulation performed with other magnetic field strengths are given in Appendix A in Figs. A.6– A.8.

Also in this case, P_L shows a dependence on the magnetic field strength and on preferred hyperfine pumping. P_L presents a sharp drop around the Van Vleck angle $\theta = 54°$. P_L peaks around $\theta = 90°$ and $\log(R/g\Omega) = 1$ (the peak is marked with a star in Fig. 2, top), with a secondary peak around $\theta = 30°$ and $\log(R/g\Omega) = 2$. This morphology is consistent across different magnetic field strengths and angular momenta of the transitions. We observe that also P_V contours show a dependence on magnetic field strength and hyperfine transitions (Fig. 2, middle). The contour morphology shows two peaks (plus their symmetric counterparts at $\theta > 90°$) located approximately at $\log(R/g\Omega) \sim 2.5$ and $\theta \sim 50°$, and at $\log(R/g\Omega) \sim -2$ and $\theta \sim 0°$. The first one is dominant at lower B strengths (1, 3, 10 mG), while the second becomes more important at higher B (20, 30, 100 mG). As the B strength increases, some hyperfine transitions present emerging features in the ψ contours, where the polarization angles flip. For instance, in the case of $B = 10$ mG

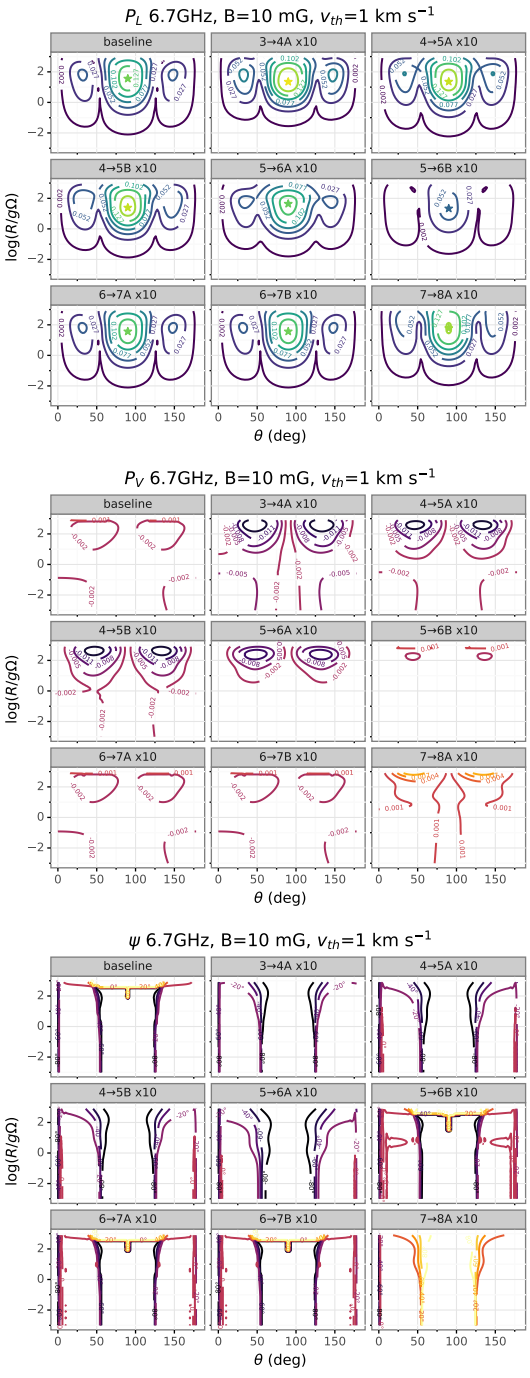

Fig. 2: 6.7 GHz methanol maser linear polarization fraction P_L (top), circular polarization fraction P_V (middle) and Linear polarization angle ψ (bottom) plotted as a function of the propagation angle θ and the rate of stimulated emission. Stars indicate the position of the peak of P_L. Magnetic field strength is 10 mG, thermal velocity width is 1 km s^{-1} and the hyperfine transitions are indicated in each panel. The panel at the top left labelled "baseline" indicates a fixed pumping rate equal for all the hyperfine transitions, while all others assume a 10× preferred pumping for the indicated $i \rightarrow j$ transition. The results of the simulation performed with other magnetic field strengths are given in Appendix A.

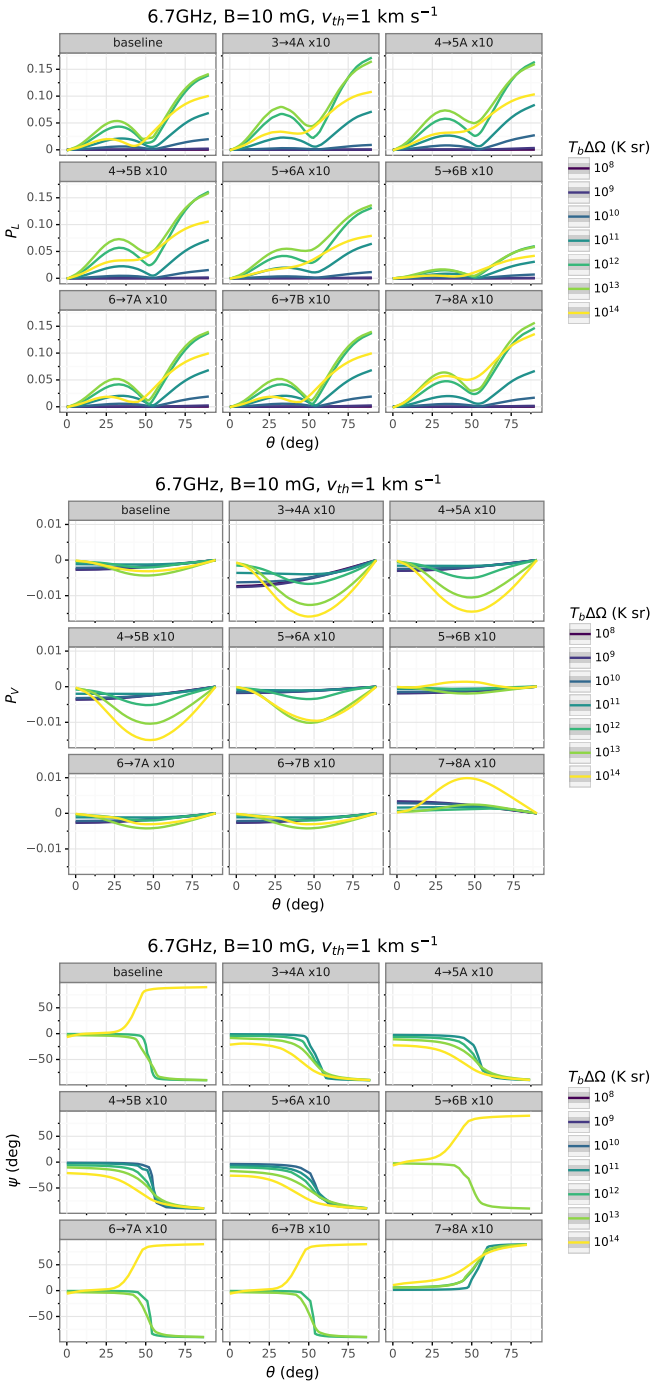

Fig. 3: 6.7 GHz methanol maser linear polarization fraction P_L (top), circular polarization fraction P_V(middle) and polarization angle ψ (bottom) plotted as a function of the propagation angle θ for different brightness temperatures. Panels as in Fig. 2.

(Fig. 2, bottom), the transition 5→6 B presents two emerging regions located at log(R/$g\Omega$) ∼ 0.5 and $\theta \sim 25°$. Similar marks appear also for magnetic fields of 30 and 100 mG in the hyperfine transition 3→4 A. We notice a 90° flip of the polarization angle ψ happening around the Van Vleck angle, and this trait becomes sharper with increasing magnetic field strength. This characteristic has been observed also for SiO and H_2O masers (Vlemmings et al. 2006; Tobin et al. 2019). Generally, when the saturation level is low (log(R/$g\Omega$) < 0), the linear polarization angle ψ appears quite stable in the range $0° < \theta < 54°$, while variations of

Table 2: P_L upper limits at $g\Omega = 10R$, for $B = 10$ mG

Maser	P_L baseline[a] %	P_L with one hyperfine transition ×10 [b]	
6.2GHz	1.9	2.2	(16→17A)
6.7GHz	2.0	2.6	(4→5A)
7.7GHz	2.5	4.1	(10→11A)
7.8GHz	2.5	4.1	(10→11A)
12GHz	2.8	3.6	(1→2B)
20.3GHz	1.7	2.1	(16→17A)
21GHz	3.2	5.6	(8→9A)
25GHz	9.5	11	(4→4A)
36GHz	2.9	3.7	(3→2A)
37.7GHz	4.6	6.1	(6→7B)
44GHz	2.2	2.8	(5→4A)
45GHz	4.1	6.2	(1→2A)
46GHz	3.5	4.5	(8→9A)

Notes. [(a)] "Baseline" indicates a fixed pumping rate equal for all the hyperfine transitions. [(b)] 10× preferred pumping for the $i \rightarrow j$ hyperfine transition indicated between parentheses.

Table 3: P_V upper limits at $g\Omega = 10R$, for $B = 10$ mG

Maser	P_V baseline[a] %	P_V with one hyperfine transition ×10	
6.2GHz	4.2	4.9	(16→17A)
6.7GHz	0.22	0.63	(3→4A)
7.7GHz	5.4	8.3	(10→11A)
7.8GHz	5.4	8.3	(10→11A)
12GHz	0.095	0.34	(1→2A)
20.3GHz	3.9	4.7	(16→17A)
21GHz	6.0	10	(8→9A)
25GHz	0.014	0.098	(4→4B)[c]
36GHz	0.011	0.05	(3→2A)
37.7GHz	8.0	10	(6→7B)
44GHz	0.011	0.056	(5→4A)
45GHz	0.011	0.055	(1→2B)
46GHz	6.7	8.3	(8→9A)

Notes. [(a)] "Baseline" indicates a fixed pumping rate equal for all the hyperfine transitions. [(b)] 10× preferred pumping for the $i \rightarrow j$ hyperfine transition indicated between parentheses. [(c)] The same level of P_V has been registered also for the 4→4A and 6→6B.

20°–40° are visible for high level of saturation. Around $\theta \sim 90°$, $\psi \sim 90°$ for almost all the saturation values.

In these plots we do not take into account the limit $g\Omega = 10R$ and therefore the strongest peak in $P_L \sim 0.2$ and $P_V \sim 0.02$, registered for the hyperfine transition 3→4 A, are due to non-Zeeman effects.

In Fig. 3 the linear and circular polarization fraction and the polarization angle are plotted as functions of the propagation angle θ for different brightness temperatures in a magnetic field $B = 10$ mG. From Fig. 1, we know that for the 6.7 GHz methanol maser $g\Omega = 10R$ happens around $T_B\Delta\Omega \sim 10^{10}$ K sr. When $T_B\Delta\Omega > 10^{10}$ K sr and $g\Omega << 10R$, the maser starts to saturate and some non-Zeeman effects (such as the rotation of the symmetry axis) can arise. P_L decreases approaching the Van Vleck angle from both smaller and greater angles, and at the Van Vleck angle P_L has a minimum. This behaviour is maintained across different levels of saturation. We note that P_L reaches its highest values when θ is greater than Van Vleck angle and for $T_B\Delta\Omega \sim 10^{12} - 10^{13}$ K sr.

Looking at the circular polarization profile, when $T_B\Delta\Omega < 10^{10}$ K sr, the maser is not saturated and P_V decreases for increasing θ, following the cosine profile described by Watson & Wyld (2001). In this regime P_V can be directly related to the magnetic field strength. When the maser saturates and $T_B\Delta\Omega > 10^{10}$ K sr, a rotation of the symmetry axis might arise, and P_V is not linked anymore to magnetic field strength. In Fig. A.5 we plot the cosine (dotted line) for different $T_B\Delta\Omega$ (solid line) to show this behaviour. We also observe an inversion of the linear polarization angle corresponding to the Van Vleck angle, which is sharp for $T_B\Delta\Omega < 10^{10}$ K sr and it becomes smoother with increasing brightness temperatures.

We also produced spectra of the 6.7 GHz methanol maser for different levels of saturation. We observe that the line broadens as the maser starts to saturate. Also the Stokes Q, U and V intensify for high saturation levels. It is also interesting to observe that, when preferred pumping is acting, a flip of the S-shape profile of the circular polarization can be observed between different hyperfine transitions. The S-shaped Stokes V profile in Fig. A.13 for the 3→4 A transition has the same shape as for the baseline profile in Fig. A.12, but the profile reverses for the 8→7 A transition in Fig. A.14. All Stokes parameters are plotted and several propagation angles θ are taken into account, assuming a magnetic field of 10 mG and v=1 km s^{-1}.

In addition, we investigated anisotropic pumping and found, as already noticed for SiO masers (Lankhaar & Vlemmings 2019), an increase of linear polarization fraction up to 100%. In light of methanol maser pumping, the amount of anisotropy that can occur is low, and since such a high level of linear polarization has never been observed, we expect that anisotropic pumping can be considered less important for methanol masers than for SiO masers. Anisotropic pumping in SiO masers occurs primarily through the absorption of IR radiation from a nearby central stellar object. Methanol masers are either pumped collisionally (class I) or radiatively (class II). Collisional pumping generally does not introduce any anisotropy in the molecular states. The radiative pumping of class II masers can be anisotropic, albeit less so than compared to the case of SiO masers, since it occurs through co-spatial dust. Additionally, the high density of class II masers de-polarizes the molecular states (Lankhaar & Vlemmings 2020), resulting in generally low degrees of anisotropic pumping. We also investigated the effect of amplification of a background polarized emission and we found that it does not contribute significantly to the linear polarization fraction unless that background emission itself is already polarized at a high enough level.

3.2. Other methanol maser transitions

For the other methanol maser transitions we investigated P_L and P_V as a function of the maser luminosity for five different θ values and magnetic fields of 10, 20 and 30 mG. In case of 25 GHz methanol maser we investigated also a magnetic field of 100 mG. All the well-known maser transitions are modelled using the N&W94 code that can treat non-Zeeman effects (see Tab. 1), and only the lesser known transitions like 6.2, 7.7, 7.8, 20.3, 20.9, 37.7 and 46 GHz, have been investigated with the N&W92 code. N&W92 code can not deal with non-Zeeman effects, and therefore the simulations stop at $g\Omega = 10R$. Within this limit

they behave like the other masers modelled with the N&W94 code.

In general, also at these other frequencies, P_L and P_V show a dependence on the hyperfine transitions, on the magnetic field strength and on the angle θ, although less so for P_V compared to P_L unless the magnetic field is very high (∼100 mG) or a hyperfine is preferentially pumped by a large degree (∼100 times), consistent with our results for 6.7 GHz masers reported in Sec. 3.1. We confirm also for these transitions that hyperfine preferred pumping can influence the polarization fraction. In Tables 2 and 3 we report P_L and P_V for these maser transition, in case of $B = 10$ mG and taken at $g\Omega = 10R$. Usually the maximum value of P_L and P_V is reached for $\theta = 90°$ and $\theta = 0°$, respectively. In the case of the 25GHz maser, the maximum in P_V is registered for the hyperfines 4→4 A and B and 6→6 B, that are the transitions where the g-factors are highest. The plots with the results of the simulations for the 6.2 GHz baseline in a magnetic field $B = 10$ mG are given in Appendix A in Fig. A.2.

Contour plots were produced only for simulations made with the N&W94 code. The 12, 25, 36, 44, 45 GHz masers show contours similar to the 6.7 GHz. P_L and P_V typically present the same morphology reported for the 6.7 GHz with a dependence on the magnetic field strength and hyperfine transitions. The P_L peaks are located in the same positions registered for the 6.7 GHz, around $\theta = 90°$ and $\log(R/g\Omega) = 1$ around $\theta = 30°$ and $\log(R/g\Omega) = 2$. The P_V peaks are situated approximately at $\log(R/g\Omega) \sim 2.5$ and $\theta \sim 50°$, and at $\log(R/g\Omega) \sim -2$ and $\theta \sim 0°$. Also for these masers, the peaks become more evident as the magnetic field strength increases. The polarization angle shows a flip of 90° around the Van Vleck angle. Generally, ψ presents a region of stability in a range $0° < \theta < 54°$ around $-2 < \log(R/g\Omega) < 0$. This region in the 25 GHz maser is limited only to the area around $\log(R/g\Omega) \sim -2$.

Also for these transitions we observe high levels of P_L and P_V due to non-Zeeman effects. When the maser is not saturated, P_V decreases for increasing θ, as predicted by Watson & Wyld (2001), while for saturated masers the curve do not follow the cosines. We show this effect in Fig. A.5 for the baselines of the 6.2, 6.7, 25 and 45 GHz masers. In the case of the 6.2 GHz maser we report the values until $R/g\Omega = 10$, and we see that all T_B are following the cosine curve and non-Zeeman effects are not present. On the contrary, for the three other masers, we can see that the P_V curves for high brightness temperatures and high levels of saturation do not decrease with increasing θ, instead they peak and show non-Zeeman effects that can lead to an overestimate of the magnetic field.

We identify also in these masers an inversion of the linear polarization angle close to the Van Vleck angle, which is sharp when the masers start to saturate and becomes smoother with increasing brightness temperatures.

Looking at the circular polarization fraction of 25, 36, 44 and 45 GHz they appear stable also for $T_B\Delta\Omega$ above $R/g\Omega = 10$. As an example, in the case of the 25 GHz maser, we obtain at $R/g\Omega = 10$ a $T_B\Delta\Omega \sim 10^9$K sr for B=10 mG. Here the P_L starts to increase while P_V keeps its stability until $T_B\Delta\Omega \sim 10^{10}$ K sr . Therefore, it might be that for P_V, non-Zeeman effects become dominant only for T_B higher than those where P_L is sensible. However, from Fig A.5, the 25 GHz maser already presents at $T_B\Delta\Omega \sim 10^{10}$ K sr a curve that slightly deviates from the cosine, indicating that some non-Zeeman effects are already acting. Also for the other masers we observe similar deviations.

3.3. 6.2 GHz methanol maser

Of the masers studied here, the 6.2 GHz maser recently discovered by Breen et al. (2019) presents the largest hyperfine split of ∼ 1 km s^{-1}. The two peaks appear quite similar in intensity. In order to investigate the two hyperfine components, we ran the models for thermal line widths $v_{th} = 1$, 1.25 and 1.50 km s^{-1} and we give the results of the simulations in Fig. A.15. We see that for v_{th} =1 km s^{-1} the two components are separated and they start to blend for v_{th} =1.25 km s^{-1}. At v_{th} =1.5 km s^{-1} the two hyperfines appear totally blended in one single line.

This case illustrates why it is complicated to detect the different hyperfine components of methanol masers at other frequencies. To observe the hyperfine components it is necessary to have an intrinsic thermal line width that is less that the hyperfine split (v_{th} <1.25 km s^{-1} in this case), otherwise we can only detect one single blended component. However, when the split is large enough with respect to the intrinsic thermal line width, our simulations predict that multiple components can be observed.

4. Discussion

4.1. Comparison between models and observations

Within the limit $g\Omega = 10R$, our model predicts linear and circular polarization fractions that can be considered upper limits, and any polarization above them will likely include some non-Zeeman contributions. We compared P_L and P_V observed in methanol masers (Table 1) with the results of our simulations (Tables 2 and 3 for $B = 10$ mG). In general we noticed that linear polarization fraction predictions are mostly lower than the observed values, even for magnetic fields higher than 10 mG, while in the case of circular polarization fractions we often observe predictions higher than the observed values. In the following part we will discuss each transition, comparing observations and models and taking into account brightness temperatures, magnetic fields and the presence of non-Zeeman effects.

4.1.1. 6.7 GHz methanol masers

We compared the results of our simulations with 6.7 GHz maser observations from Breen et al. (2019), Surcis et al. (2019) and Surcis et al. (2009) (these masers are reported in Table 1). These works reported high P_L of the order of 7.5%, 8.1% and 4.5% respectively. We selected some extreme measurements of P_L from the works of Surcis et al. and 6.7 GHz methanol masers typically present lower values ranging from 1% to 4% (Surcis et al. 2019, and references therein).

We now discuss the possible action of non-Zeeman effects on the three selected 6.7 GHz methanol masers and reported in Table 1. The observed brightness temperatures range between 10^{11}–10^{13} K and, assuming $\Delta\Omega \sim 10^{-2}$ sr, the $T_B\Delta\Omega$ obtained from observations vary between 10^9–10^{11} K sr. Our 6.7 GHz methanol maser model gives $T_B\Delta\Omega \sim 10^{10}$ K sr at $g\Omega = 10R$, for a magnetic field of 10 mG, but when the magnetic field strength reaches $B = 100$ mG, the limit increases by one order of magnitude becoming $T_B\Delta\Omega \sim 10^{11}$ K sr. This indicates that the selected masers are not affected by the rotation of the symmetry axis, but might be influenced by other non-Zeeman contributions (e.g. a rotating magnetic field along the maser direction) that can occur even at modest T_B. Thus, if we consider $g\Omega = 10R$ as an upper limit, we can estimate that the maximum brightness temperature reachable before being severely affected

by non-Zeeman effects is $\sim 10^{12}$ K (for $B = 10$ mG) or $\sim 10^{13}$ K (for $B = 100$ mG).

For the 6.7 GHz maser transition observed by Breen et al. (2019), we do not have information regarding the magnetic field strength, but T_B inferred from observations is within the limit $g\Omega = 10R$ for both $B = 10$ mG and $B = 100$ mG. According to our model, such a high level of P_L can be generated by a high B or by a specific hyperfine preferred pumping or by a combination of both. Indeed for $B = 100$ mG, it is possible to reach a $P_L \sim 10\%$ (see Fig. A.1, e.g. with the transitions $4 \rightarrow 5$A and B). In addition, under the action of different preferred pumping, from 3 to 100 times over the baseline level, the amount of linear and circular polarization fraction increases and can reach, depending on the angle, up to 7.5%, even in $B = 10$ mG (see Fig. A.3 and Fig. A.4). Breen et al. (2019) also reported a $P_V = 0.5\%$ that is within the values reported by our model for a $B = 10$ mG (Table 3). However $P_V = 0.5\%$ is also consistent with the results of our model considering a $B = 100$ mG and an hyperfine preferred pumping on the transition $4 \rightarrow 5$A. In any case, given the high P_L observed, we can not exclude the influence of some non-Zeeman effects. Since T_B inferred from observations is within the $g\Omega = 10R$ limit, we can rule out a rotation of the symmetry axis, but it could be possible to have a contribution in P_V of $\sim 0.14\%$ due to magnetic field changes along the maser path (as described in Sect. 1.1.2).

Surcis et al. (2019) reported $B > 182$ mG, $P_L = 8.1\%$ and $P_V = 2.1\%$ for the maser feature WH3(OH).22 and the T_B inferred from their observations is $\sim 10^{13}$ K. These values are in agreement with our models for a magnetic field $B = 100$ mG and within the $g\Omega = 10R$ limit. However, since P_L is high, we cannot exclude minor non-Zeeman contributions affecting P_V, that could count ~0.16% due to magnetic field changes along the maser path (Sect. 1.1.2).

In the case of W75N, Surcis et al. (2009) estimated a $T_B\Delta\Omega < 10^9$ K sr and, given $\Delta\Omega \sim 10^{-1}$ sr and a maser angular size of 7 mas, they obtained $\theta = 70°$ and B=50 mG. They also registered a $P_L = 4.5\%$ and a P_V=0.2%. As for W3(OH), this value of P_L and P_V can be generated under the action of different degrees of hyperfine preferred pumping and $B = 10$–100 mG. If we exclude a different pointing direction of the magnetic field, hyperfine preferred pumping could be probable in the case of W75N: indeed, if we compare the S-shape profile of the observed V spectrum with the synthetic one, we see that the emission detected by Surcis et al. (2009) is compatible with a preferred pumping on hyperfine transitions $7 \rightarrow 8$A, or $6 \rightarrow 7$A. It is notable that these are not the same hyperfines of Tab. 2 and Tab. 3.

4.1.2. 25 GHz methanol masers

Sarma & Momjian (2020) observed 25 GHz methanol masers in two different epochs in the OMC–1 region. They reported for the two detections a level of $P_V \sim 0.3\%$ and $P_V \sim 0.4\%$, and, based on the low $T_B\Delta\Omega$, conclude that non-Zeeman effect likely contributes little to this percentage. From our models in case of B=100 mG and for $T_B\Delta\Omega \sim 10^6$ K sr, we confirm that non-Zeeman effects are neglegible and we found a $P_V \sim 1\%$, for the strongest hyperfine transitions, also considered by Sarma & Momjian (2020). While this value is still higher than the measured values, we note that our simulations were run for $v_{th} = 1$ km s^{-1} . At $T_B\Delta\Omega \sim 10^6$ K sr, our spectra have a FWHM linewidth of slightly less than half that of the observed spectrum (0.24 km s^{-1} vs. 0.53 km s^{-1}). Since in the normal Zeeman interpretation, the fractional polarization is inversely proportional to the line-width this indicates that the observed polarization in OMC-1 can indeed be the result of a magnetic field of ~100 mG.

From our models in case of B=30 mG we derive at the $g\Omega = 10R$ limit a value of $T_B\Delta\Omega \sim 10^9$ K sr and P_V ~0.2% for the same hyperfine transitions considered by Sarma & Momjian (2020). While this indicates that a level of circular polarization can be reached that is similar to the observed level for a smaller magnetic field strength, this only occurs for values of $T_B\Delta\Omega$ that are more than three orders of magnitude larger than estimated from the observations. In that case, part of P_V originates from non-Zeeman effects, which do not contribute at the lower observed $T_B\Delta\Omega$. Alternatively, if the maser spot size is overestimated, and thus T_B underestimated, and/or $\Delta\Omega$ is significantly higher, non-Zeeman effects might after all be present in the observed signal. However, currently, there are no observational indications that either is the case, leading us to conclude that the normal Zeeman analysis performed in Sarma & Momjian (2020) can be used and that the 25 GHz methanol masers trace a shock enhanced magnetic field.

4.1.3. 36 GHz methanol masers

Sarma & Momjian (2009) detected 36 GHz methanol masers across the M8E region with a $P_V \sim 0.1\%$ and estimated a magnetic field $B_{LOS} \sim 20$–30 mG. Also Breen et al. (2019) reported a very low level in both linear and circular polarization fractions, lower than 0.5%. From our simulations, we confirm a low P_V for this maser and we found an agreement with the observations, since the $3 \rightarrow 2$ A hyperfine can produce a $P_V \sim 0.1\%$ for a magnetic field $B_{LOS} \sim 20$–30 mG. In addition, comparing the V spectrum observed by Sarma & Momjian (2009) with the one produced by our models, we find that also in this case preferred pumping might have acted on the hyperfine transition $3 \rightarrow 2$ A; this transition indeed generates an evident S-shape profile — one that appears much less prominent in the baseline case.

For this maser at the $g\Omega = 10R$, we obtain a $T_B\Delta\Omega \sim 10^9$ K sr, and assuming the same $\Delta\Omega \sim 10^{-2}$ sr, this leads to a limit in brightness temperature of $\sim 10^{11}$ K, which is above the range constrained from observations. Given the low level of P_L observed by Breen et al. (2019), we exclude a significant non-Zeeman contribution for this maser emission.

4.1.4. 44 GHz methanol masers

Momjian & Sarma (2019) observed 44.1 GHz methanol masers in the DR21W star forming region, detecting a $P_V \sim 0.05\%$. They considered the hyperfine transition $5 \rightarrow 4$ A and constrained a lower limit for the magnetic field $B_{LOS} \sim 25$ mG. In our model we also obtain $P_V \sim 0.056\%$ when this hyperfine transition is preferably pumped and for a magnetic field of 10 mG. For a $B = 30$ mG the resulting $P_V \sim 0.1\%$. In both the case, B is in the same order of magnitude of the one suggested by Momjian & Sarma (2019). However the observed spectra show the presence of multiple components and therefore we cannot totally exclude other combinations of hyperfines producing this emission. Even so, the synthetic V spectra of the $5 \rightarrow 4$ A present a S-shaped profile that is in agreement with the observed one. Breen et al. (2019) observed P_L and P_V less than 0.5%, but from our simulations the predicted maximum $P_L \sim 3\%$. Given the low level of P_L observed by Breen et al. (2019), we can rule out any contribution due to magnetic field changes along the maser path. By comparing T_B from observations and model, we can exclude also a rotation of the symmetry axis. From our model

$T_B\Delta\Omega \sim 10^9$ K sr at $g\Omega = 10R$ limit for $B = 10$ mG. Therefore if $\Delta\Omega \sim 10^{-2}$ sr, the maximum brightness temperature reachable to exclude the rotation of the symmetric axis is $\sim 10^{11}$ K which is higher than the observed ones.

4.1.5. 45 GHz methanol masers

From our simulations we obtain $T_B\Delta\Omega \sim 10^9$ K sr at the $g\Omega = 10R$ limit for $B = 10$ mG; thus we estimate a maximum brightness temperature reachable to exclude a rotation of the symmetric axis of $T_B \sim 10^{11}$ K, which is several orders of magnitude higher than that observed by Breen et al. (2019). We also note that the level of P_L and P_V predicted by our model for $B = 10$ mG are higher than the one detected by Breen et al. (2019).

4.1.6. Other methanol masers

Other methanol masers transitions presenting high level of P_L were detected at 6.2, 7.7, 7.8, 21, 37.7, 46 GHz and at 20.3 GHz by Breen et al. (2019) and MacLeod et al. (2019) respectively. We could not model non-Zeeman effects because the simulations for these transitions were performed with the N&W92 code, limited to $g\Omega = 10R$. However looking at the $T_B\Delta\Omega$ inferred from our models and comparing them with the ones estimated from observations, for all these masers we can exclude a rotation of the symmetry axis.

For the 6.2 GHz maser, the observed $P_L \sim 7\%$ has not been predicted by our simulations, while, the predicted P_V is instead much higher than the one detected by Breen et al. (2019). In this case we cannot exclude the contribution of non-Zeeman effects enhancing linear polarization. Looking at 7.7 GHz and 7.8 GHz masers, the detected P_L and P_V are lower than the predicted ones. For the 21 GHz, the observed P_L is $\sim 7\%$ and our models show $P_L \sim 6\%$ in case of $B = 30$ mG and for the hyperfine transitions 8→9 A pumped 10 times more than the baseline. 37.7 GHz observations shows high P_L values which are almost in agreement with our model for a $B = 10$ mG, while 46 GHz presents P_L higher than the predicted one. We can not exclude the action of non-Zeeman effects or a combination of hyperfine preferred pumping at higher B strength.

Since these masers are likely arising from the same region of the protostar (Breen et al. 2019; MacLeod et al. 2019), one possible explanation for these high observed levels of P_L could be due to the action of a magnetic field $\gtrsim 100$ mG or to specific hyperfine pumping or to the synergy of both. More observations will probably help in understanding which process in ongoing in this region, by measuring P_V and by inferring the B strength.

4.2. Reversed profile in circular polarization spectra

Dall'Olio et al. (2017) observed a reversed profile in 6.7 GHz methanol maser I and V spectra detected between two different epochs in the high mass protostar IRAS 18089-1732. In these observations the V spectra presented two S-shape profiles, one being the opposite of the other. One of the possible explanations given by these authors to interpret the reversed I profiles and opposite circular polarization was the presence of two hyperfine components of the 6.7 GHz methanol transition $5_1 \rightarrow 6_0$. Under this hypothesis, one hyperfine transition would be preferred over the other in one epoch, and vice versa in the following epoch. Our simulations shows that this possibility can occur if the two components of the spectra are given by the hyperfine transitions $3 \rightarrow 4$ A and $7 \rightarrow 8$ A, as shown in Figs. A.12, A.13, and A.14. It can also occur when the two hyperfine transitions $6 \rightarrow 7$ A and B are simultaneously preferentially pumped. However, since the same effect could be also due either to a flip in the magnetic field strength intrinsic to the source (Vlemmings et al. 2009) or to different and blended masers, originating in two places lying along the same line of sight (e.g. Momjian & Sarma 2017), further methanol masers observations are needed to help in understanding the magnetic field action and its link on preferred hyperfine pumping.

4.3. 6.2 GHz methanol maser and its hyperfine splitting

As reported in Sect. 3.3, our simulations show that it is possible to observe the hyperfine splitting of two components for the 6.2 GHz methanol maser, when the thermal line width $v_{th} \lesssim 1.25$ km s^{-1}. Therefore, we showed that a splitting significantly larger than the intrinsic thermal line width is required to actually observe the split. In addition, the first detection of this maser was performed by Breen et al. (2019), but from their single dish observations it is impossible to discern if the features in the spectra are clear signs of hyperfine splitting or not. Further high angular resolution observations might help to observe the splitting between these two hyperfine components.

5. Conclusions

Masers can be considered useful tools to infer magnetic field properties in star forming regions, and by observing linear and circular polarization we can study the magnetic field morphology and strength in different parts of the protostar.

We ran simulations using the radiative transfer CHAMP code, for several magnetic field strengths, hyperfine components, and pumping efficiencies. We explored the polarization properties of some observed methanol maser transitions, considering newly calculated methanol Landé factors and preferred hyperfine pumping. We also investigated the action of non-Zeeman effects, that can contaminate magnetic field estimates.

We noticed a dependence of the linear polarization fraction on the magnetic field strength and on the hyperfine transitions. Also the circular polarization fraction presents a dependence on the hyperfine transitions. We found that distinct hyperfine components react to the magnetic field differently. Thus, in case of preferred hyperfine pumping, high levels of linear and circular polarization can be produced, explaining some of the high P_L and P_V observed. We discussed some of the peculiar features seen in the S-shape of the observed V-profiles. Comparing T_B obtained from our models with the observations, we argue that methanol masers do not appear affected by a rotation of the symmetry axis. However other non-Zeeman effects might arise also at modest T_B and they need to be considered in the study of magnetic fields.

A possible way to constrain these effects is represented by observing polarized emission from other maser transitions expected to arise from the same region. Observations of only P_L would be used to determine the direction of the magnetic field that can be parallel or perpendicular to the linear polarization vector; however, the observed P_L values will be consistent with several models of preferred hyperfine pumping and it will be impossible to discern which hyperfine preferred pumping might be occurring. P_L will allow to achieve estimate on saturation level and the possible effect of magnetic field rotation on measured P_V. Single observations of masers presenting only P_V, can be

used to derive lower limits of magnetic field strength and can be helpful to determine and discuss the most probable hyperfine transitions acting. By simultaneous observations of P_L and P_V, if possible also in different transitions, one can confidently rule out the presence of non-Zeeman contributions or estimate their actual action. Also a more accurate knowledge of the maser beaming angle $\Delta\Omega$ and thus more precise measurement of the brightness temperature T_B will help to understand the amount of non-Zeeman contributions and on which hyperfine transitions they are more relevant.

We showed an hyperfine splitting occurring between two components of the 6.2 GHz methanol maser, when $v_{th} < 1.25$ km s^{-1}. We have seen that a splitting significantly larger than the intrinsic thermal line width is required to detect the splitting between the hyperfine components.

Therefore further high angular resolution observations of methanol masers are necessary to understand how hyperfine preferred pumping works. The comparison between these observational details will be fundamental to better understand the simultaneous action of magnetic fields and preferred pumping.

Acknowledgements. We thank the referee for the insightful comments and accurate suggestions that have contributed to the improvement of this work. Simulations were performed on resources at the Chalmers Centre for Computational Science and Engineering (C3SE) provided by the Swedish National Infrastructure for Computing (SNIC).

Table A.1: Characteristics of hyperfine transitions for 6.2 GHz methanol maser

Hyperfine transition	Hyperfine shift (Hz)	g-factor ($s^{-1}mG^{-1}$)	A_{i-j} s^{-1}
16 → 17 A	-11180	-0.8094	9.247×10^{-10}
17 → 18 A	11720	-0.0335	4.624×10^{-10}
17 → 18 B	-12410	0.0048	4.624×10^{-10}
18 → 19 A	10830	0.6945	9.226×10^{-10}
16 → 17 B	-11730	-0.8094	9.247×10^{-10}
17 → 18 C	12240	-0.0335	4.624×10^{-10}
17 → 18 D	-12810	0.0048	4.634×10^{-10}
18 → 19 B	11210	0.6945	9.226×10^{-10}

Table A.2: Characteristics of hyperfine transitions for 6.7 GHz methanol maser

Hyperfine transition	Hyperfine shift (Hz)	g-factor ($s^{-1}mG^{-1}$)	A_{i-j} s^{-1}
7 → 8 A	2500	2.9712	1.03×10^{-9}
6 → 7 A	-4397	1.6416	1.04×10^{-9}
6 → 7 B	3541	1.4112	1.02×10^{-9}
5 → 6 A	-2889	-0.8016	1.01×10^{-9}
5 → 6 B	3015	0.0096	1.00×10^{-9}
4 → 5 A	1240	-2.9376	1.06×10^{-9}
4 → 5 B	-2835	-3.2496	1.03×10^{-9}
3 → 4 A	-4417	-7.1472	1.08×10^{-9}

Table A.3: Characteristics of hyperfine transitions for 7.7 GHz methanol maser

Hyperfine transition	Hyperfine shift (Hz)	g-factor ($s^{-1}mG^{-1}$)	A_{i-j} s^{-1}
10 → 11 A	10970	-2.9311	7.063×10^{-10}
11 → 12 A	-3300	-1.5661	4.395×10^{-10}
11 → 12 B	7710	-1.6428	4.355×10^{-10}
12 → 13 A	-7390	-0.4215	3.483×10^{-10}
12 → 13 B	6680	-0.5460	3.483×10^{-10}
13 → 14 A	-9370	0.5460	4.305×10^{-10}
13 → 14 B	8230	0.4071	4.345×10^{-10}
14 → 15 A	-8830	1.3075	6.982×10^{-10}

Table A.4: Characteristics of hyperfine transitions for 7.8 GHz methanol maser

Hyperfine transition	Hyperfine shift (Hz)	g-factor ($s^{-1}mG^{-1}$)	A_{i-j} s^{-1}
10 → 11 A	10870	-2.9263	7.464×10^{-10}
11 → 12 A	-3230	-1.5613	4.656×10^{-10}
11 → 12 B	7620	-1.6380	4.613×10^{-10}
12 → 13 A	-7320	-0.4167	3.690×10^{-10}
12 → 13 B	6600	-0.5412	3.690×10^{-10}
13 → 14 A	-9290	0.5508	4.560×10^{-10}
13 → 14 B	8160	0.4119	4.603×10^{-10}
14 → 15 A	-8750	1.3123	7.396×10^{-10}

Table A.5: Characteristics of hyperfine transitions for 12 GHz methanol maser

Hyperfine transition	Hyperfine shift (Hz)	g-factor ($s^{-1}mG^{-1}$)	A_{i-j} s^{-1}
3 → 4 A	-4965	3.4180	0.737×10^{-8}
2 → 3 A	-4802	0.6911	0.752×10^{-8}
2 → 3 B	-1475	-0.5592	0.732×10^{-8}
1 → 2 A	7978	-6.8670	0.803×10^{-8}
3 → 4 B	-6106	2.9400	0.737×10^{-8}
2 → 3 C	5847	1.8470	0.610×10^{-8}
2 → 3 D	-1475	-1.0430	0.571×10^{-8}
1 → 2 B	-3263	-6.6920	0.803×10^{-8}

Table A.6: Characteristics of hyperfine transitions for 20.3 GHz methanol maser

Hyperfine transition	Hyperfine shift (Hz)	g-factor ($s^{-1}mG^{-1}$)	A_{i-j} s^{-1}
16 → 17	10020	-1.2884	1.197×10^{-8}
17 → 18	-8010	-0.4933	5.984×10^{-9}
17 → 18	9100	-0.5029	5.984×10^{-9}
18 → 19	-9710	0.2059	1.194×10^{-8}
16 → 17	10020	-1.2884	1.197×10^{-8}
17 → 18	-8010	-0.4933	5.984×10^{-9}
17 → 18	9100	-0.5029	5.984×10^{-9}
18 → 19	-9710	0.2059	1.194×10^{-8}

Appendix A: Appendix

References

Breen, S. L., Sobolev, A. M., Kaczmarek, J. F., et al. 2019, ApJ, 876, L25
Burns, J. O., Owen, F. N., & Rudnick, L. 1979, AJ, 84, 1683
Caswell, J. L., Kramer, B. H., & Reynolds, J. E. 2011, MNRAS, 414, 1914
Crutcher, R. M. & Kemball, A. J. 2019, Frontiers in Astronomy and Space Sciences, 6, 66
Dall'Olio, D., Vlemmings, W. H. T., Surcis, G., et al. 2017, A&A, 607, A111
Dinh-v-Trung. 2009, MNRAS, 399, 1495
Etoka, S., Cohen, R. J., & Gray, M. D. 2005, MNRAS, 360, 1162
Fiebig, D. & Guesten, R. 1989, A&A, 214, 333
Fish, V. L., Reid, M. J., Menten, K. M., & Pillai, T. 2006, A&A, 458, 485
Green, J. A., McClure-Griffiths, N. M., Caswell, J. L., Robishaw, T., & Harvey-Smith, L. 2012, MNRAS, 425, 2530
Houde, M. 2014, ApJ, 795, 27
Houde, M., Hezareh, T., Jones, S., & Rajabi, F. 2013, ApJ, 764, 24
Hunter, T. R., Brogan, C. L., MacLeod, G. C., et al. 2018, ApJ, 854, 170
Lankhaar, B., Groenenboom, G. C., & van der Avoird, A. 2016, J. Chem. Phys., 145, 244301
Lankhaar, B. & Vlemmings, W. 2019, A&A, 628, A14
Lankhaar, B. & Vlemmings, W. 2020, A&A, 636, A14
Lankhaar, B., Vlemmings, W., Surcis, G., et al. 2018, Nature Astronomy, 2, 145
MacLeod, G. C., Sugiyama, K., Hunter, T. R., et al. 2019, MNRAS, 489, 3981
Momjian, E. & Sarma, A. P. 2017, ApJ, 834, 168
Momjian, E. & Sarma, A. P. 2019, ApJ, 872, 12
Moscadelli, L., Menten, K. M., Walmsley, C. M., & Reid, M. J. 2003, ApJ, 583, 776
Nedoluha, G. E. & Watson, W. D. 1990a, ApJ, 354, 660
Nedoluha, G. E. & Watson, W. D. 1990b, ApJ, 361, 653
Nedoluha, G. E. & Watson, W. D. 1992, ApJ, 384, 185
Nedoluha, G. E. & Watson, W. D. 1994, ApJ, 423, 394
Pérez-Sánchez, A. F. & Vlemmings, W. H. T. 2013, A&A, 551, A15
Sarma, A. P. & Momjian, E. 2009, ApJ, 705, L176
Sarma, A. P. & Momjian, E. 2020, ApJ, 890, 6
Sarma, A. P., Troland, T. H., & Romney, J. D. 2001, ApJ, 554, L217
Sarma, A. P., Troland, T. H., Romney, J. D., & Huynh, T. H. 2008, ApJ, 674, 295
Surcis, G., Vlemmings, W. H. T., Curiel, S., et al. 2011a, A&A, 527, A48
Surcis, G., Vlemmings, W. H. T., Dodson, R., & van Langevelde, H. J. 2009, A&A, 506, 757
Surcis, G., Vlemmings, W. H. T., Torres, R. M., van Langevelde, H. J., & Hutawarakorn Kramer, B. 2011b, A&A, 533, A47
Surcis, G., Vlemmings, W. H. T., van Langevelde, H. J., & Hutawarakorn Kramer, B. 2012, A&A, 541, A47
Surcis, G., Vlemmings, W. H. T., van Langevelde, H. J., Hutawarakorn Kramer, B., & Bartkiewicz, A. 2019, A&A, 623, A130
Surcis, G., Vlemmings, W. H. T., van Langevelde, H. J., Hutawarakorn Kramer, B., & Quiroga-Nuñez, L. H. 2013, A&A, 556, A73

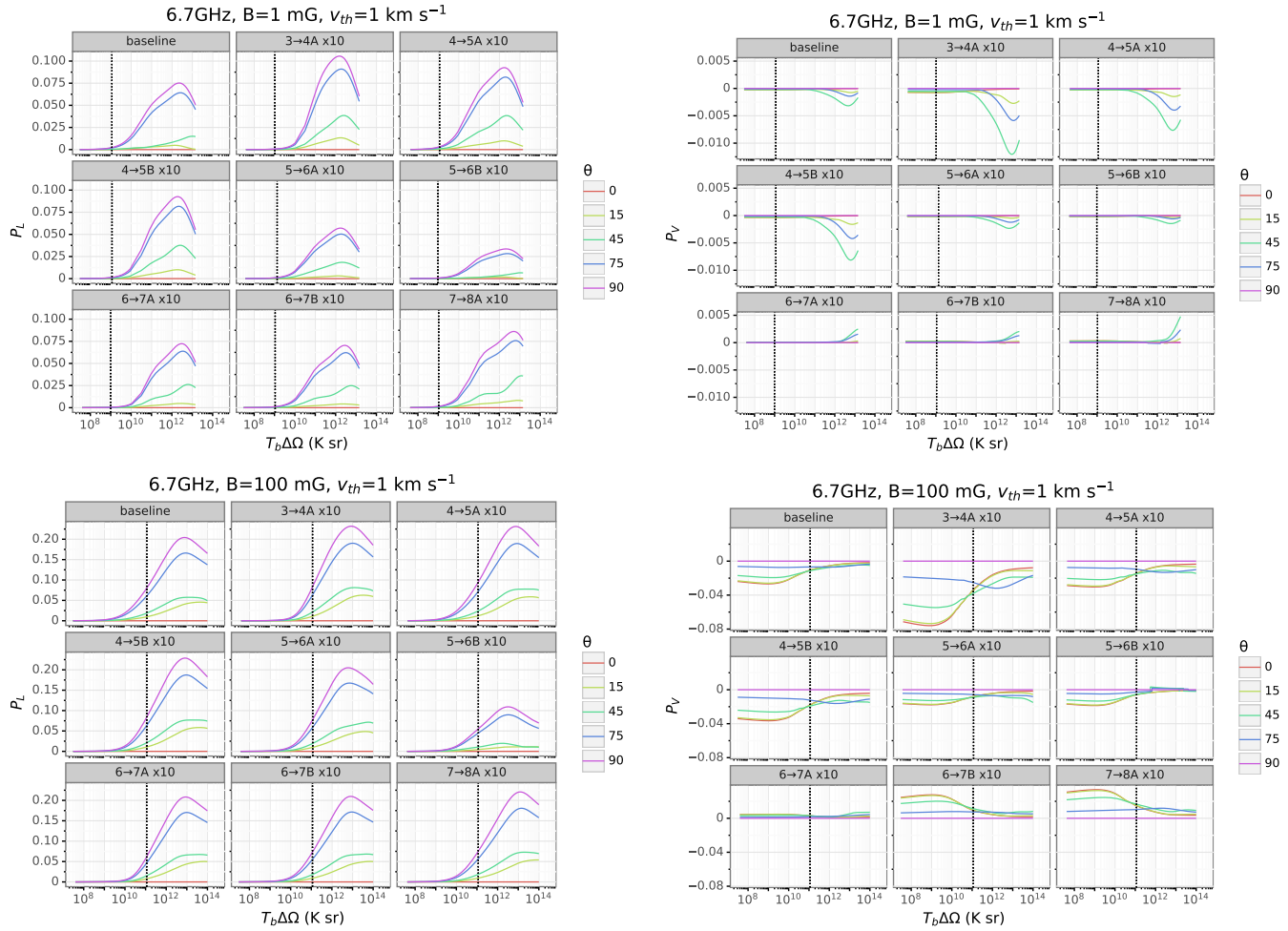

Fig. A.1: 6.7 GHz methanol maser linear and circular polarization fraction as a function of the maser luminosity for five different θ. The vertical line marks $T_B\Delta\Omega$ where $g\Omega = 10R$. Magnetic field strength is 1 and 100 mG, thermal velocity width is 1 km s^{-1} and the hyperfine transitions are indicated in each panel. The panel at the top left labelled "baseline" indicates a fixed pumping rate equal for all the hyperfine transitions, while all others assume a 10× preferred pumping for the indicated $i \rightarrow j$ transition.

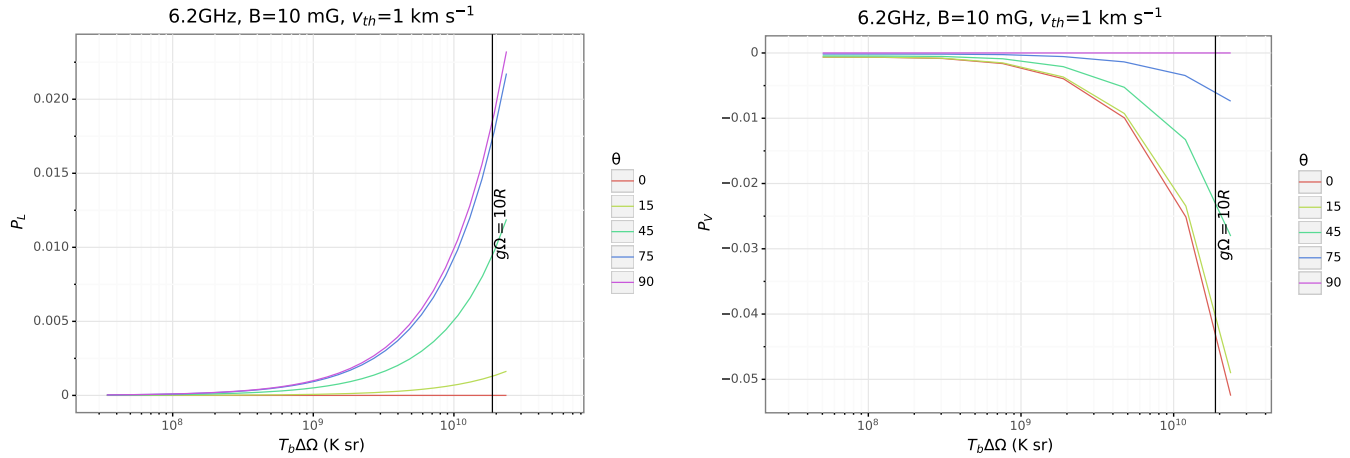

Fig. A.2: 6.2 GHz methanol maser baseline. Linear and circular polarization fraction as a function of the maser luminosity for five different θ. The vertical line marks $T_B\Delta\Omega$ where $g\Omega = 10R$. Magnetic field strength is 10 mG, thermal velocity width is 1 km s^{-1}.

Tobin, T. L., Kemball, A. J., & Gray, M. D. 2019, ApJ, 871, 189
Vlemmings, W. H. T. 2007, in IAU Symposium, Vol. 242, Astrophysical Masers and their Environments, ed. J. M. Chapman & W. A. Baan, 37–46
Vlemmings, W. H. T. 2008, A&A, 484, 773
Vlemmings, W. H. T., Diamond, P. J., van Langevelde, H. J., & Torrelles, J. M. 2006, A&A, 448, 597
Vlemmings, W. H. T., Goedhart, S., & Gaylard, M. J. 2009, A&A, 500, L9
Vlemmings, W. H. T., Surcis, G., Torstensson, K. J. E., & van Langevelde, H. J.

Table A.7: Characteristics of hyperfine transitions for 21 GHz methanol maser

Hyperfine transition	Hyperfine shift (Hz)	g-factor ($s^{-1}mG^{-1}$)	A_{i-j} s^{-1}
8 → 9 A	-21710	-2.5719	3.373×10^{-8}
9 → 10 A	-1730	-1.0297	2.018×10^{-8}
9 → 10 B	-13560	-0.8238	1.991×10^{-8}
10 → 11 A	6920	0.1581	1.660×10^{-8}
10 → 11 B	-7210	0.6801	1.663×10^{-8}
11 → 12 A	5150	2.3803	1.445×10^{-8}
11 → 12 B	4990	0.7040	1.449×10^{-8}
12 → 13 A	18650	2.4953	3.327×10^{-8}

Table A.8: Characteristics of hyperfine transitions for 25 GHz methanol maser

Hyperfine transition	Hyperfine shift (Hz)	g-factor ($s^{-1}mG^{-1}$)	A_{i-j} s^{-1}
6 → 6 A	-26	4.4480	5.570×10^{-8}
5 → 5 A	4223	0.2830	5.538×10^{-8}
5 → 5 B	-1070	0.3896	5.533×10^{-8}
4 → 4 A	1462	-5.4850	5.500×10^{-8}
6 → 6 B	3754	4.5990	5.570×10^{-8}
5 → 5 C	-271	0.1131	5.537×10^{-8}
5 → 5 D	-1070	0.3393	5.532×10^{-8}
4 → 4 B	-3784	-5.4290	5.500×10^{-8}

Table A.9: Characteristics of hyperfine transitions for 36 GHz methanol maser

Hyperfine transition	Hyperfine shift (Hz)	g-factor ($s^{-1}mG^{-1}$)	A_{i-j} s^{-1}
5 → 4 A	5402.	3.054	15.238×10^{-8}
4 → 3 A	-4791.	1.093	13.009×10^{-8}
4 → 3 B	-3395.	-1.722	12.615×10^{-8}
3 → 2 A	-3032.	-4.524	13.994×10^{-8}
5 → 4 B	4042.	2.664	15.238×10^{-8}
4 → 3 C	4303.	0.3519	14.595×10^{-8}
4 → 3 D	-3395.	-0.4712	14.469×10^{-8}
3 → 2 B	-6802.	-4.423	13.995×10^{-8}

2010, MNRAS, 404, 134
Vlemmings, W. H. T., Torres, R. M., & Dodson, R. 2011, A&A, 529, A95
Watson, W. 2008, in Cosmic Agitator: Magnetic Fields in the Galaxy, 21
Watson, W. D. & Wyld, H. W. 2001, ApJ, 558, L55
Western, L. R. & Watson, W. D. 1984, ApJ, 285, 158
Wiebe, D. S. & Watson, W. D. 1998, ApJ, 503, L71
Zeeman, P. 1897, ApJ, 5, 332

Table A.10: Characteristics of hyperfine transitions for 37.7 GHz methanol maser

Hyperfine transition	Hyperfine shift (Hz)	g-factor ($s^{-1}mG^{-1}$)	A_{i-j} s^{-1}
6 → 7 A	8220	-2.2989	9.638×10^{-8}
7 → 8 A	-6150	-0.1341	4.831×10^{-8}
7 → 8 B	8110	-0.6178	4.875×10^{-8}
8 → 9 A	-7750	1.1207	9.594×10^{-8}
6 → 7 B	1550	-2.2989	9.638×10^{-8}
7 → 8 C	-350	-0.3448	4.842×10^{-8}
7 → 8 D	1090	-0.4023	4.842×10^{-8}
8 → 9 B	-1380	1.1207	9.594×10^{-8}

Table A.11: Characteristics of hyperfine transitions for 44 GHz methanol maser

Hyperfine transition	Hyperfine shift (Hz)	g-factor ($s^{-1}mG^{-1}$)	A_{i-j} s^{-1}
9 → 8 A	-2444	2.5950	27.449×10^{-8}
8 → 7 A	3934	1.2755	27.116×10^{-8}
8 → 7 B	-3216	1.3006	26.796×10^{-8}
7 → 6 A	2897	-0.6786	26.285×10^{-8}
7 → 6 B	-2897	-0.1005	26.078×10^{-8}
6 → 5 A	-1684	-2.5321	26.407×10^{-8}
6 → 5 B	2863	-2.7395	25.874×10^{-8}
5 → 4 A	3898	-5.7805	25.913×10^{-8}

Table A.12: Characteristics of hyperfine transitions for 45 GHz methanol maser

Hyperfine transition	Hyperfine shift (Hz)	g-factor ($s^{-1}mG^{-1}$)	A_{i-j} s^{-1}
1 → 2 A	-3850	-6.7387	2.512×10^{-7}
2 → 3 A	540	-1.8104	1.352×10^{-7}
2 → 3 B	-4250	1.8008	1.679×10^{-7}
3 → 4 A	5870	3.3622	2.884×10^{-7}
1 → 2 B	-5600	-6.7387	2.512×10^{-7}
2 → 3 C	1940	0.1868	1.556×10^{-7}
2 → 3 D	-2030	-0.2012	1.455×10^{-7}
3 → 4 B	3780	3.3622	2.884×10^{-7}

Table A.13: Characteristics of hyperfine transitions for 46 GHz methanol maser

Hyperfine transition	Hyperfine shift (Hz)	g-factor ($s^{-1}mG^{-1}$)	A_{i-j} s^{-1}
8 → 9 A	7930	-1.9828	1.531×10^{-7}
9 → 10 A	-5650	-0.4454	7.674×10^{-8}
9 → 10 B	7300	-0.5268	7.674×10^{-8}
10 → 11 A	-7570	0.7328	1.524×10^{-7}
8 → 9 B	8930	-1.9828	1.531×10^{-7}
9 → 10 C	-6560	-0.4454	7.674×10^{-8}
9 → 10 D	8110	-0.5268	7.674×10^{-8}
10 → 11 B	-8300	0.7328	1.524×10^{-7}

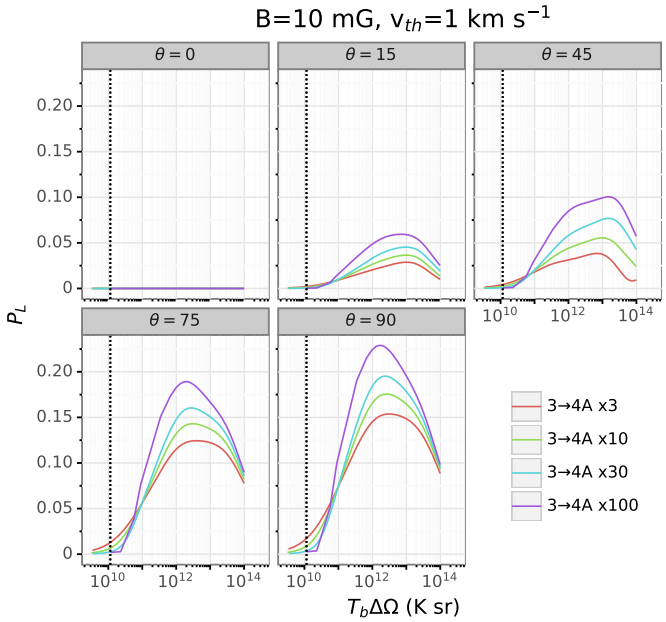

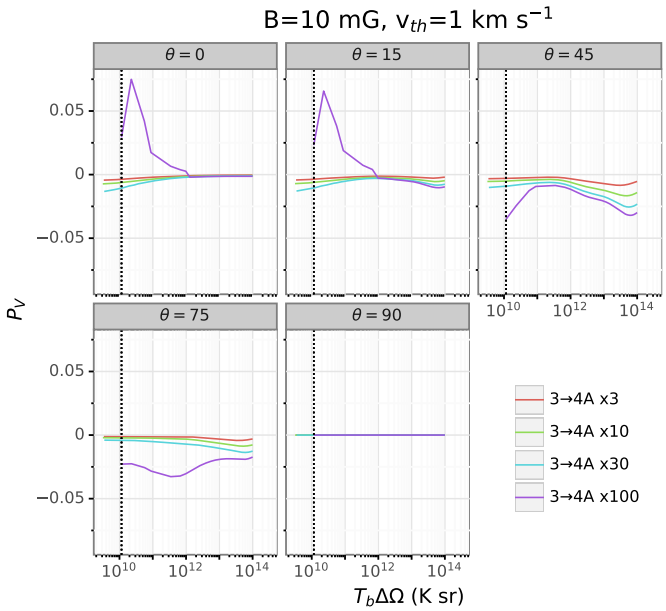

Fig. A.3: 6.7 GHz methanol maser linear and circular polarization fraction as a function of the maser luminosity. Colours indicates different degrees of preferred pumping (3, 10, 30, 100 times) for the hyperfine transition 3 → 4 A. The vertical dotted lines indicate $g\Omega = 10R$. Magnetic field strength, angle θ, and thermal width are indicated in the plot.

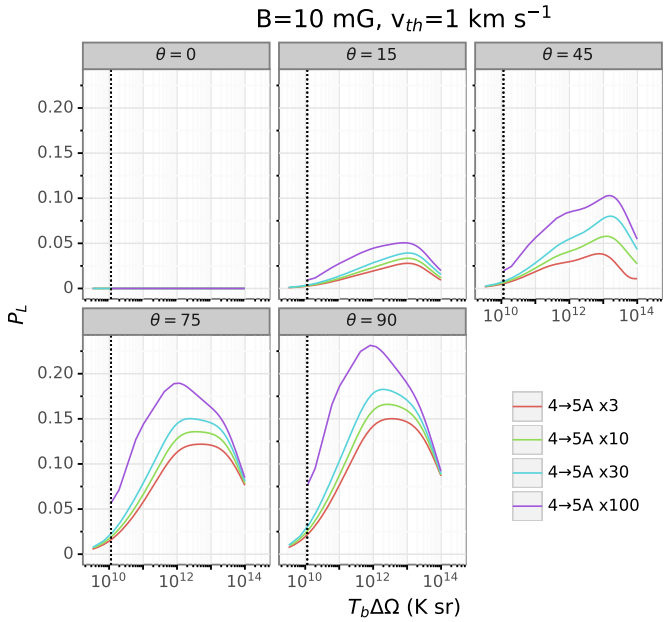

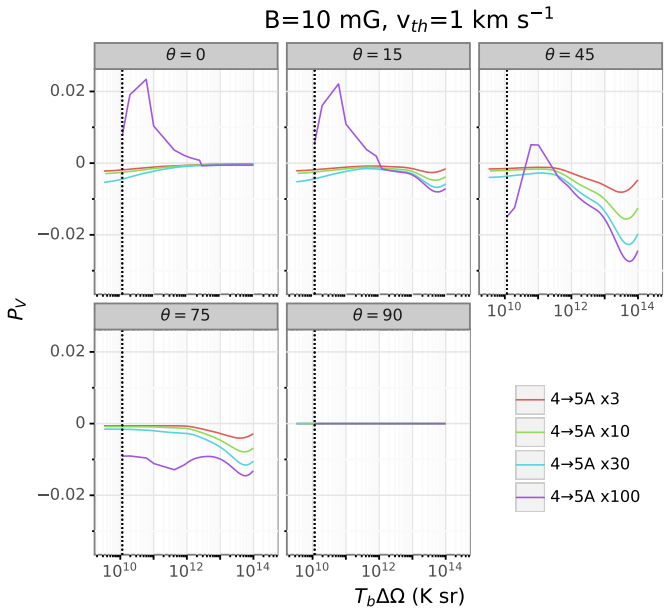

Fig. A.4: 6.7 GHz methanol maser linear and circular polarization fraction as a function of the maser luminosity. Colours indicates different degrees of preferred pumping (3, 10, 30, 100 times) for the hyperfine transition 4 → 5 A. The vertical dotted lines indicate $g\Omega = 10R$. Magnetic field strength, angle θ, and thermal width are indicated in the plot.

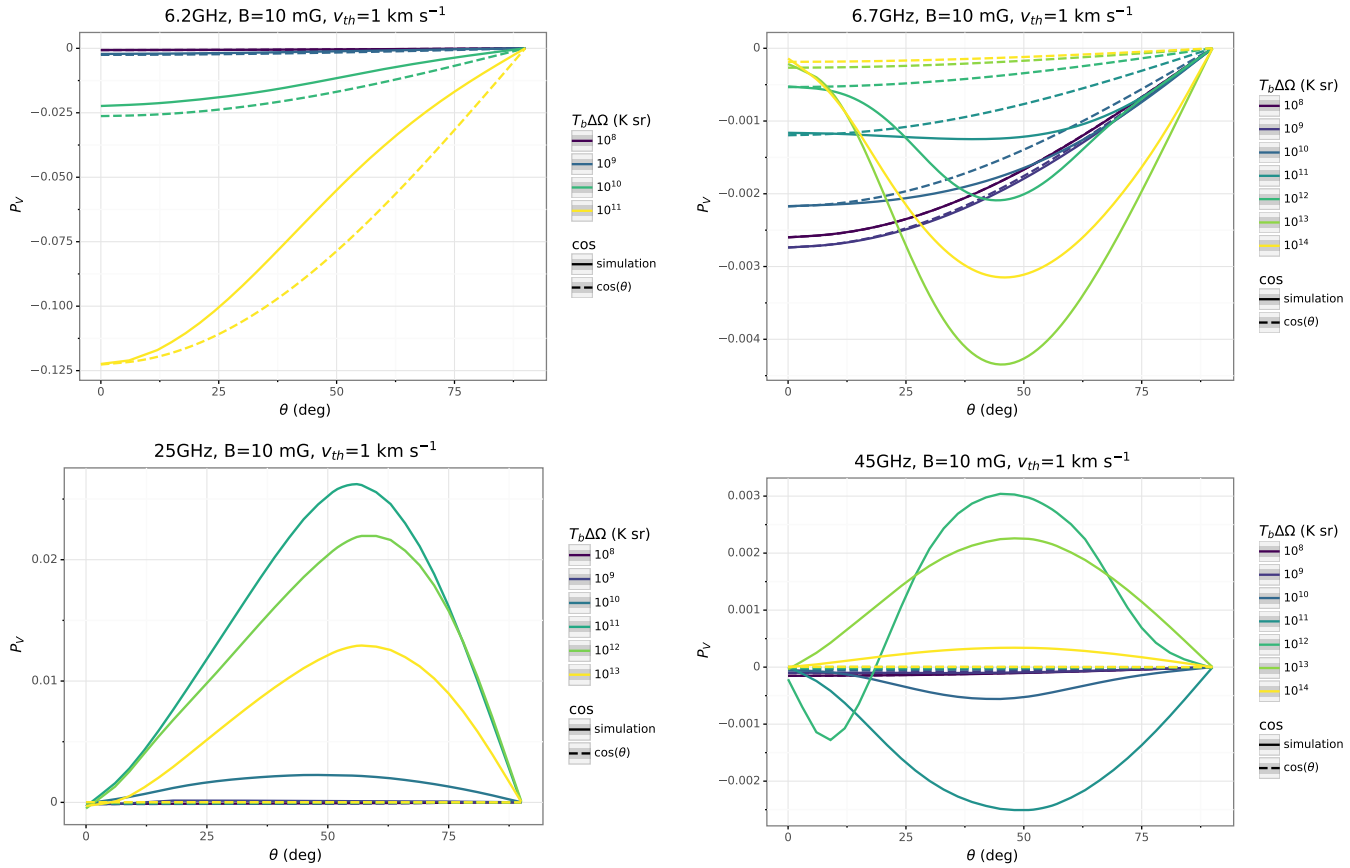

Fig. A.5: Circular polarization fraction as a function of θ for different $T_B\Delta\Omega$, for 6.2 GHz, 6.7 GHz, 25 GHz and 45 GHz methanol maser baselines. Magnetic field strength is 10 mG, thermal velocity width is 1 km s^{-1}. For the 6.2 GHz methanol maser $T_B\Delta\Omega$ corresponding to $g\Omega = 10R$ limit is $\sim 2 \times 10^{10}$ K sr; for the 6.7 GHz methanol maser $T_B\Delta\Omega$ corresponding to $g\Omega = 10R$ is $\sim 10^{10}$ K sr ; for the 25 GHz methanol maser $T_B\Delta\Omega$ corresponding to $g\Omega = 10R$ is $\sim 10^9$ K sr; for the 45 GHz methanol maser $T_B\Delta\Omega$ corresponding to $g\Omega = 10R$ is $\sim 9 \times 10^8$ K sr.

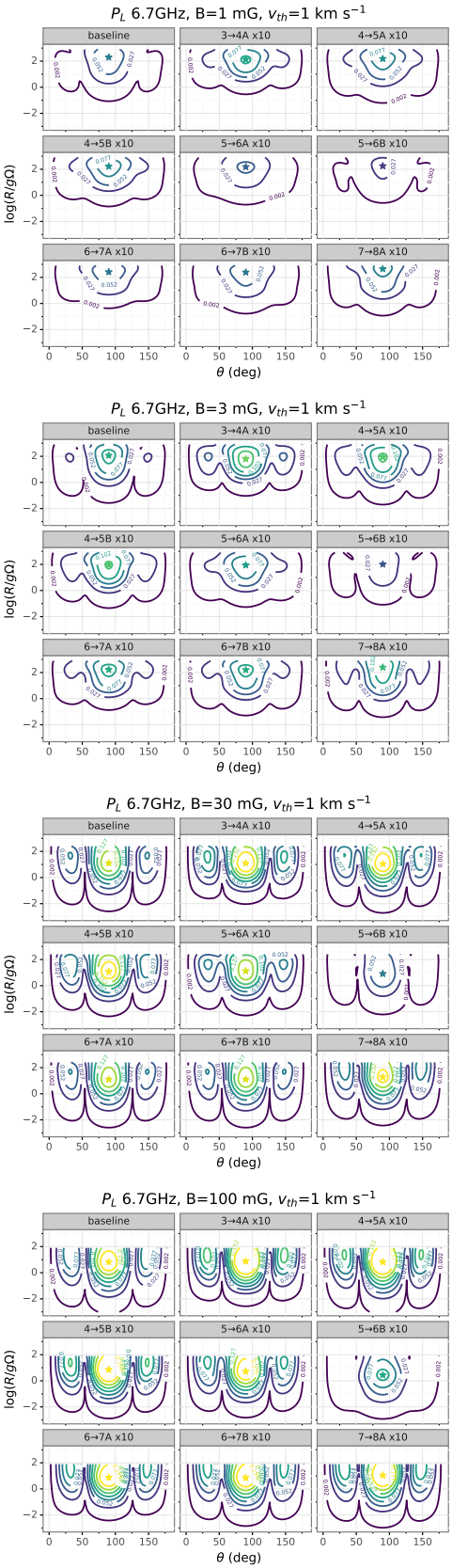

Fig. A.6: 6.7 GHz methanol maser linear polarization fraction P_L, plotted as a function of the propagation angle θ and the rate of stimulated emission. B strengths, v_{th}, and the preferred hyperfine transitions are indicated in each panel. The panel at the top left labelled "baseline" indicates a fixed pumping rate equal for all the hyperfine transitions, while all others assume a 10× preferred pumping for the indicated $i \rightarrow j$ transition.

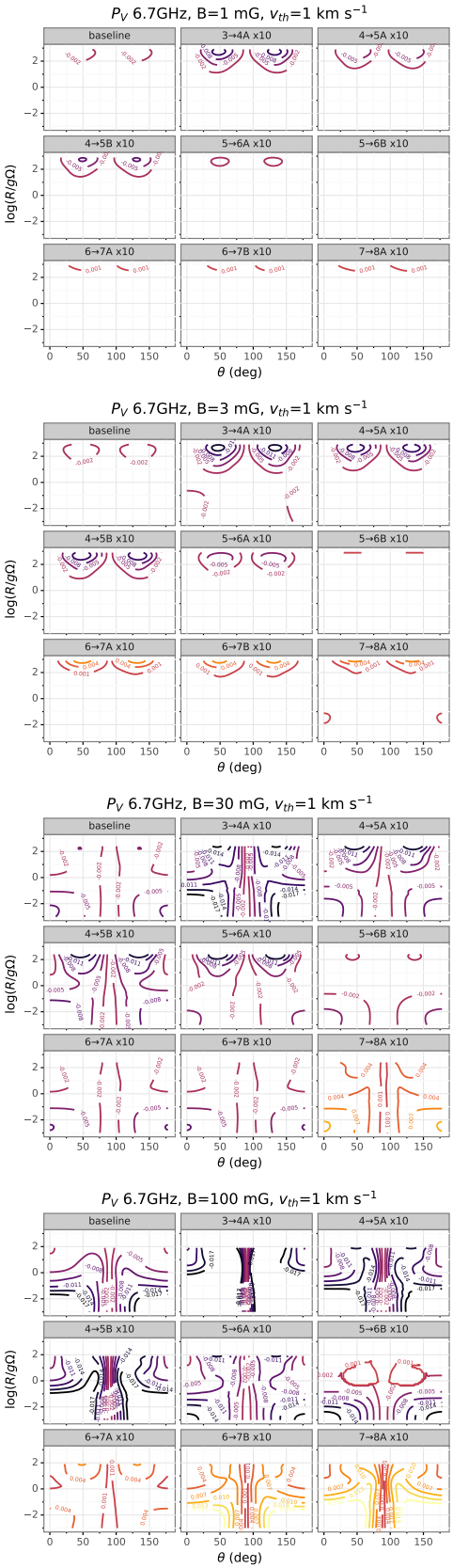

Fig. A.7: 6.7 GHz methanol maser circular polarization fraction P_V, plotted as a function of the propagation angle θ and the rate of stimulated emission. Panels as in Fig. A.6

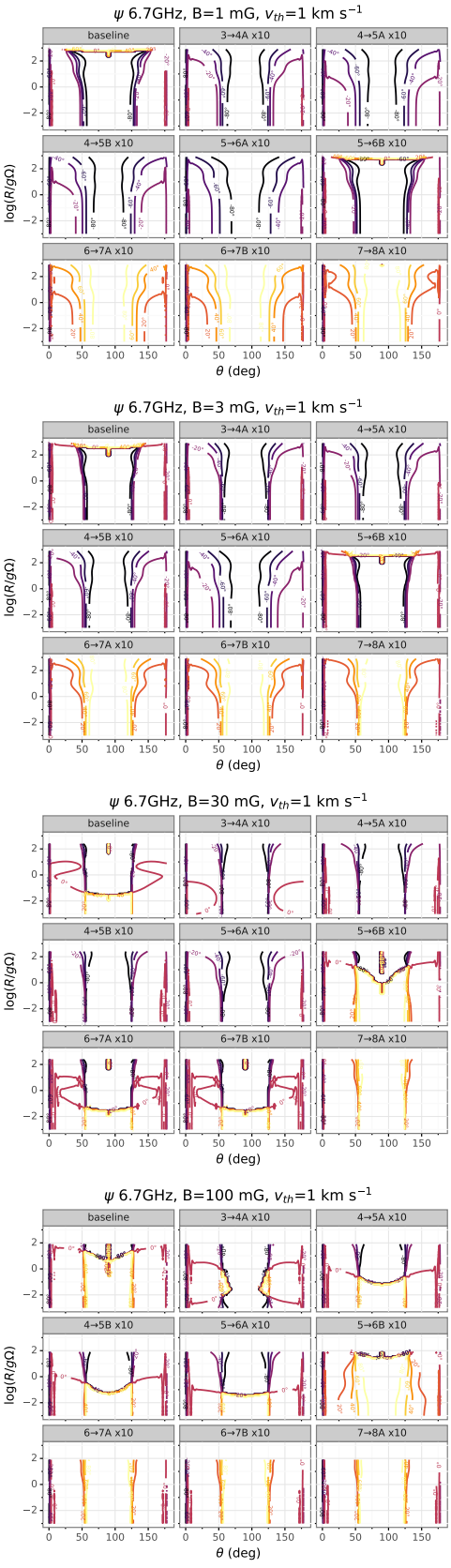

Fig. A.8: 6.7 GHz methanol maser linear polarization angle ψ, plotted as a function of the propagation angle θ and the rate of stimulated emission. Contours are plotted every 20°. Panels as in Fig. A.6

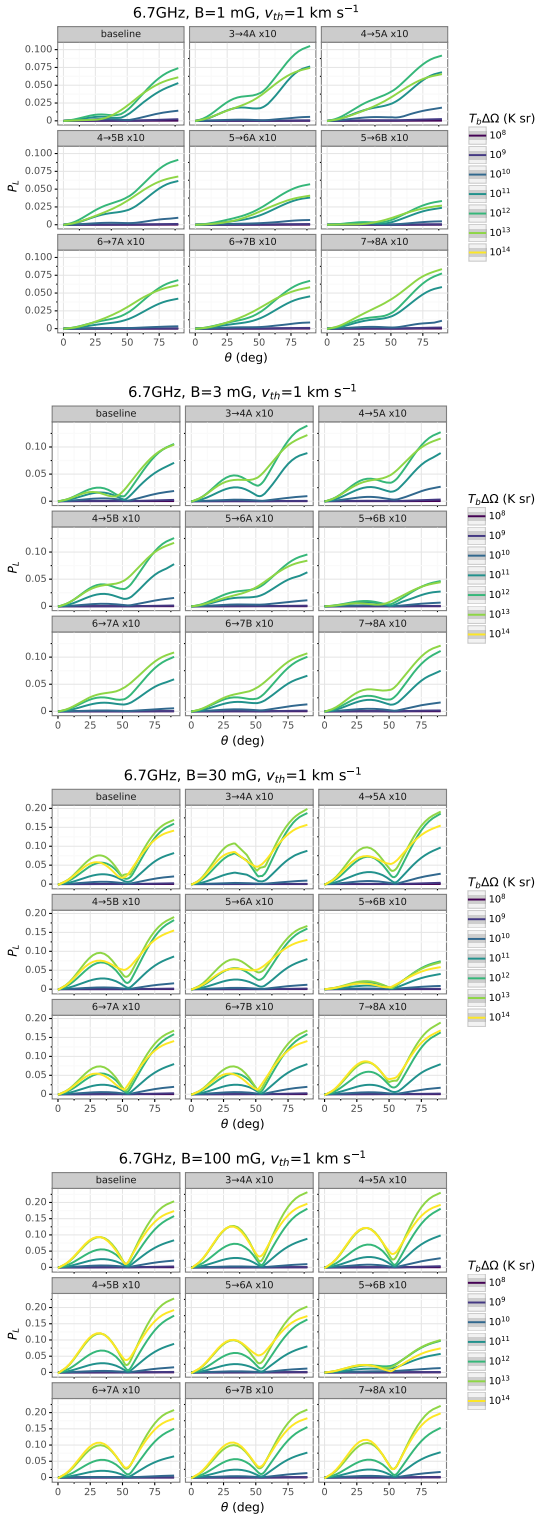

Fig. A.9: 6.7 GHz methanol maser linear polarization fraction, plotted as a function of the propagation angle θ for different brightness temperatures. B strength, v_{th} and the preferred hyperfine transitions are indicated in each panel. The panel at the top left labelled "baseline" indicates a fixed pumping rate equal for all the hyperfine transitions, while all others assume a 10× preferred pumping for the indicated $i \rightarrow j$ transition.

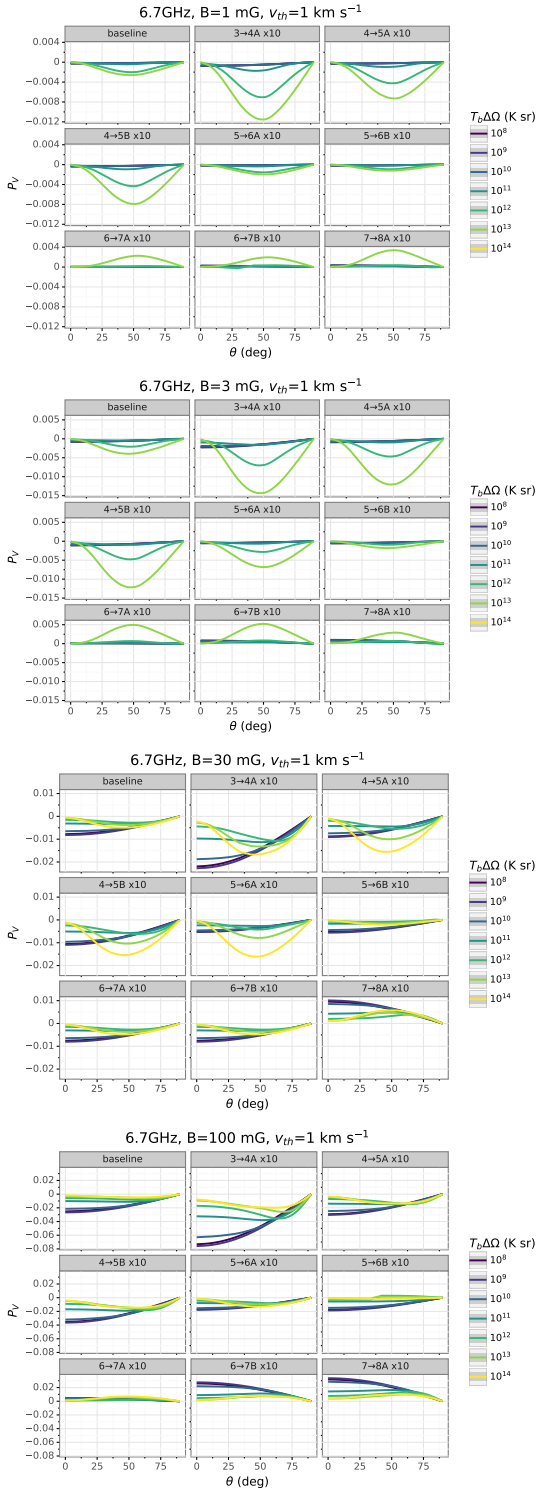

Fig. A.10: 6.7 GHz methanol maser circular polarization fraction P_V, plotted as a function of the propagation angle θ for different brightness temperatures. Panels as in Fig. A.9.

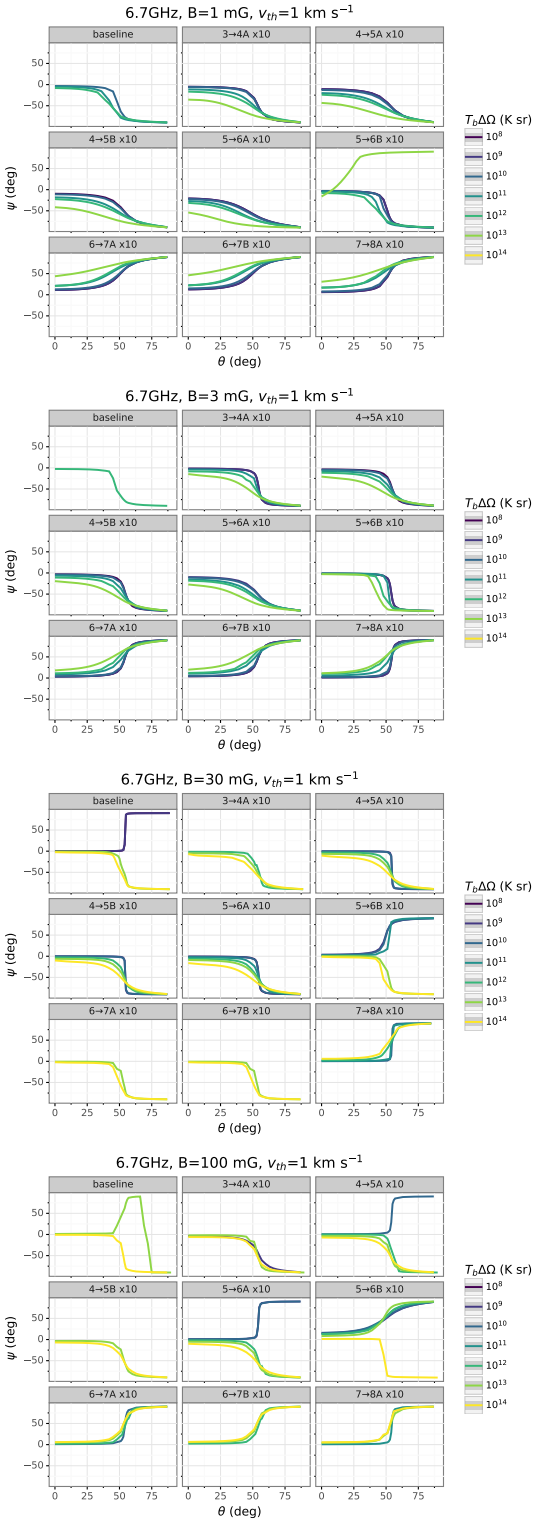

Fig. A.11: 6.7 GHz methanol maser linear polarization angle ψ, plotted as a function of the propagation angle θ for different brightness temperatures. Panels as in Fig. A.9.

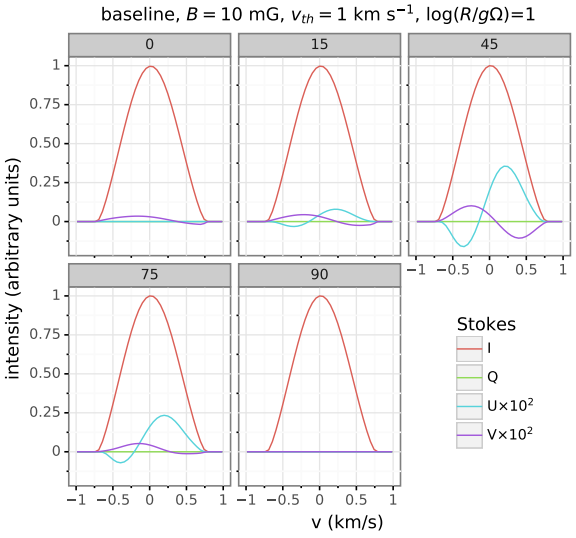

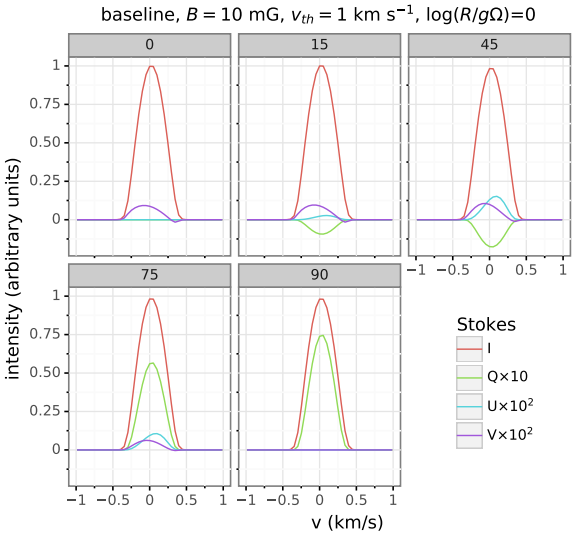

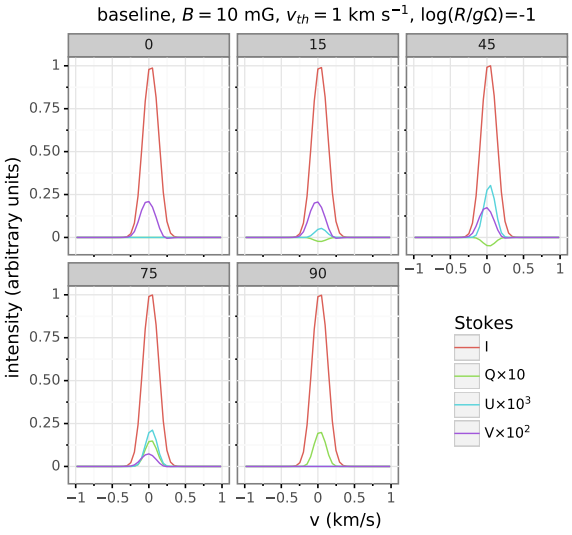

Fig. A.12: 6.7 GHz methanol maser spectra for different levels of saturation, considering all the hyperfine transitions equally pumped. Simulations were performed for stokes I, Q, U, and V, and propagation angles θ of 0, 15, 45, 75, and 90.

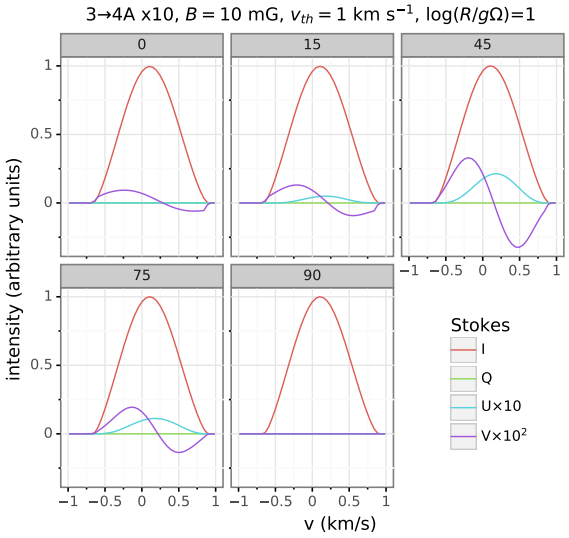

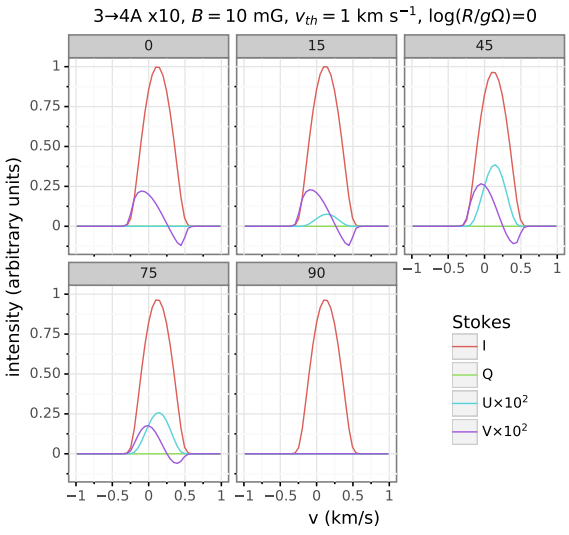

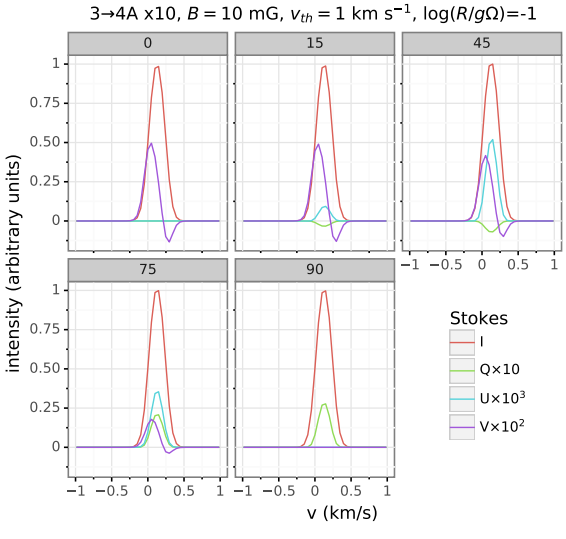

Fig. A.13: 6.7 GHz methanol maser spectra for different levels of saturation. Simulations were performed for stokes I, Q, U, and V, and propagation angles θ of 0, 15, 45, 75, and 90. Preferred pumping on the 3 → 4A hyperfine transition was applied.

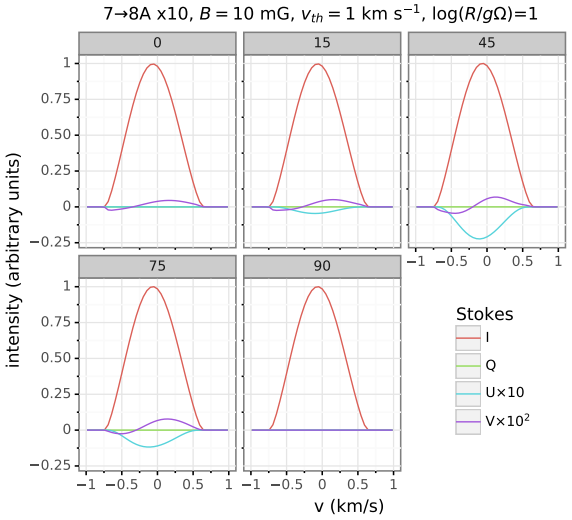

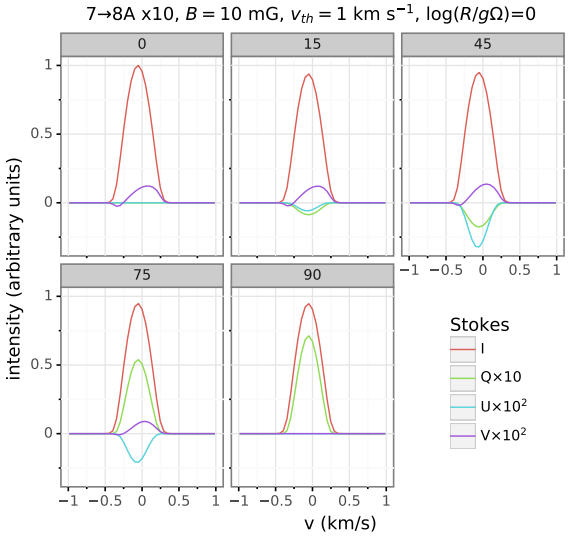

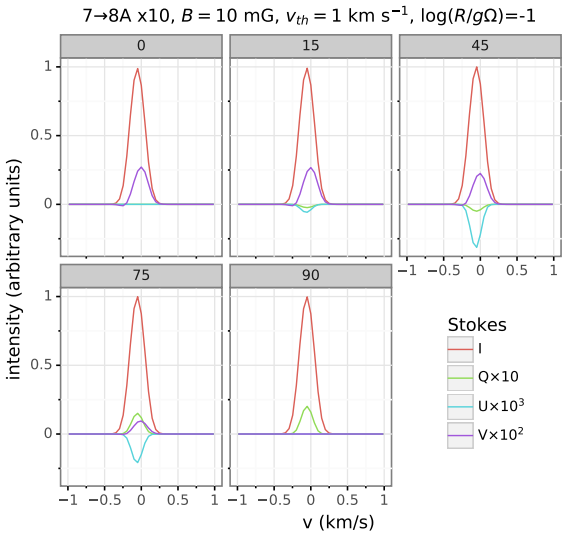

Fig. A.14: 6.7 GHz methanol maser spectra for different levels of saturation. Simulations were performed for stokes I, Q, U, and V, and for propagation angles θ of 0, 15, 45, 75 and 90. Preferred pumping on the 7 → 8A hyperfine transition was applied.

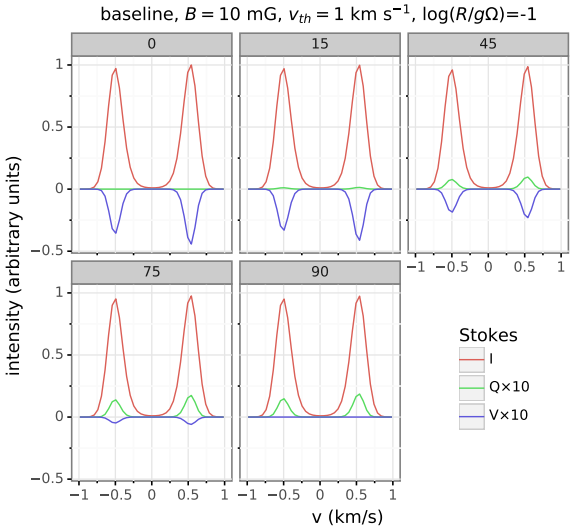

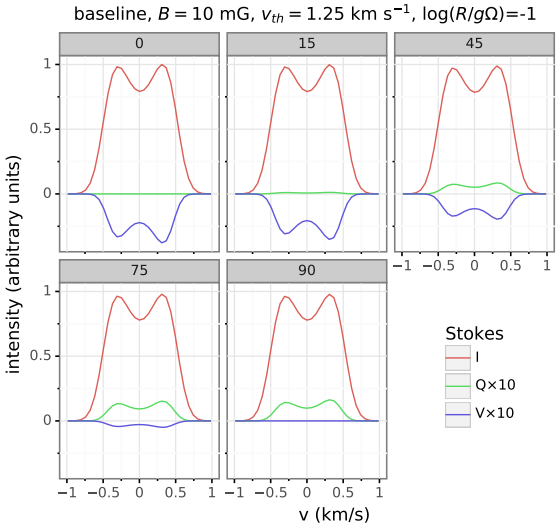

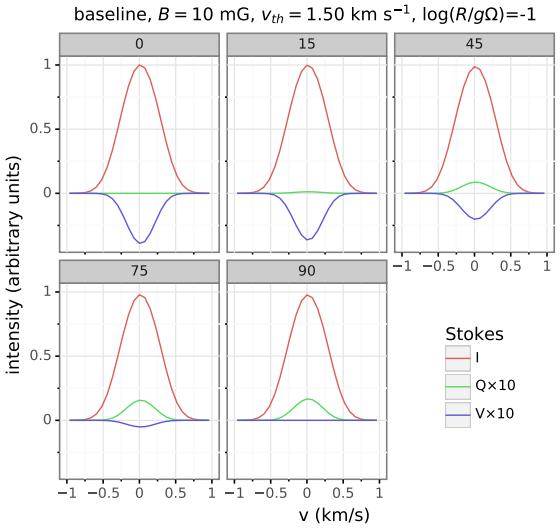

Fig. A.15: 6.2 GHz methanol maser spectra for different intrinsic thermal velocity width. Simulations were performed for stokes I, Q, U, and V, and for propagation angles θ of 0, 15, 45, 75 and 90.